Observations of a Colorado Tornado. Part I: Mesoscale Environment and Tornadogenesis

J. M. WILCZAK,* T. W. CHRISTIAN,† D. E. WOLFE,* R. J. ZAMORA,* AND B. STANKOV*

*NOAA/ERL/Wave Propagation Laboratory, Boulder, Colorado
†Cooperative Institute for Research in the Environmental Sciences (CIRES), University of Colorado/NOAA, Boulder, Colorado

(Manuscript received 11 November 1990, in final form 13 August 1991)

ABSTRACT

On 2 July 1987 a nonmesocyclone tornado was observed in northeastern Colorado during the Convection Initiation and Downburst Experiment (CINDE). This tornado, reaching F1–F2 intensity, developed under a rapidly growing convective cell, without a preceding supercell or midlevel mesocyclone being present.

The pretornado environment on 2 July is described, including observations from a triangle of wind profilers, a dense surface mesonet array, and a special balloon sounding network. Important features contributing to tornado generation include the passage of a 700-mb short-wave trough; the formation of an ~70-km diameter, terrain-induced mesoscale vortex (the Denver Cyclone) and its associated baroclinic zone; the presence of a stationary low-level convergence boundary; and the presence of low-level azimuthal shear maxima (misovortices) along the boundary.

Vorticity budget terms are calculated in the lowest 2 km AGL using a multiple-Doppler radar analysis. These terms and their spatial distributions are compared with observations of mesocyclone-associated supercell tornadoes. Results show that vorticity associated with the 2 July nonsupercell tornado was generated in a more complicated manner than that proposed by previous nonsupercell tornadogenesis theory. In particular, tilting of baroclinically generated streamwise horizontal vorticity into the vertical was important for the formation of low-level rotation, in a manner similar to that previously proposed for supercell tornadic storms.

1. Introduction

Tornadoes have traditionally been classified according to whether or not they are associated with the mesocyclone of a mature supercell storm (Davies-Jones 1986). Nonmesocyclone tornadoes occur early in the development of supercell storms, before a mesocyclone forms (Burgess and Donaldson 1979); along the gust front of mature supercell storms but outside the core of the mesocyclone (Lemon and Doswell 1979); along synoptic frontal boundaries (Carbone 1983; Wilson 1986); or along other types of convergent boundaries that are not associated with supercell convection (Brady and Szoke 1989; Szoke and Brady 1989; Wakimoto and Wilson 1989; hereafter WW89).

On the basis of their analyses, Brady and Szoke (1989) and WW89 suggested that tornadoes not associated with supercell convection form by the process of amplification of preexisting vertical vorticity through the stretching mechanism. This preexisting vertical vorticity is associated with horizontal shears occurring along surface convergence boundaries before storm development. As convective clouds grow over the convergent boundaries, low-level vertical vorticity associated with the horizontal shear is amplified through convergence at the base of the cloud updrafts, resulting in tornadogenesis.

This proposed nonsupercell tornadogenesis mechanism is fundamentally different from the current theory of supercell–mesocyclone tornadogenesis. That theory, based on observations and theoretical contributions (Davies-Jones 1984; Lilly 1982; Lemon and Doswell 1979; Barnes 1970; Browning and Landry 1963), and numerical modeling studies (Klemp and Rotunno 1983; Rotunno and Klemp 1985), suggests that the process of supercell tornadogenesis consists of 1) ambient streamwise horizontal vorticity being tilted into the vertical by a developing storm updraft, producing storm rotation that results in the generation of a midlevel mesocyclone; 2) midlevel rotation generating spiraling rain-cooled outflows to the north and west of the main updraft; 3) baroclinic generation of additional near-surface streamwise horizontal vorticity as parcels travel parallel to the isotherms in the strong thermal gradient along the rain-cooled outflow; 4) the tilting of this horizontal vorticity into the vertical by the main storm updraft; and 5) the amplification of this vertical vorticity through stretching to form the near-surface mesocyclone and its associated tornado.

Although the final step in both of these proposed mechanisms is the same (vorticity amplification through stretching) the supercell–mesocyclone mechanism, as proposed by Rotunno and Klemp (1985),

Corresponding author address: Dr. James M. Wilczak, NOAA/ERL, 325 Broadway, Boulder, CO 80303-3328.

first relies on tilting of baroclinically produced horizontal vorticity. In contrast, the nonsupercell mechanism proposed by WW89 and Brady and Szoke requires only preexistent vertical vorticity along a convergent boundary; tilting is of no importance.

The observational analyses of WW89 and Brady and Szoke (1989) that lead to the proposed nonsupercell tornado mechanism were based on surface mesonet and single-Doppler radar data. Vorticity budget analyses using multiple-Doppler radar–derived winds were not evaluated to verify the theory. An observational evaluation of the supercell tornadogenesis theory of Rotunno and Klemp (1985) was undertaken by Johnson et al. (1987). Although a buoyancy gradient with the correct orientation for the generation of streamwise horizontal vorticity was observed, verification of the theory remained inconclusive due to the sparseness of their surface observations. Brandes (1984a) applied thermodynamic retrieval techniques to Doppler radar data from two tornadic mesocyclones. The orientation of parcel streamlines relative to the retrieved buoyancy fields suggested, however, that baroclinic generation of horizontal vorticity occurred in only one of the two mesocyclones.

In this study we provide a detailed analysis of the mesoscale environment of a tornado that occurred in northeastern Colorado on 2 July 1987. This tornado, also included in the study by WW89, was observed during the Convection Initiation and Downburst Experiment (CINDE), a cooperative field program involving the Wave Propagation Laboratory (WPL) of the National Oceanic and Atmospheric Administration

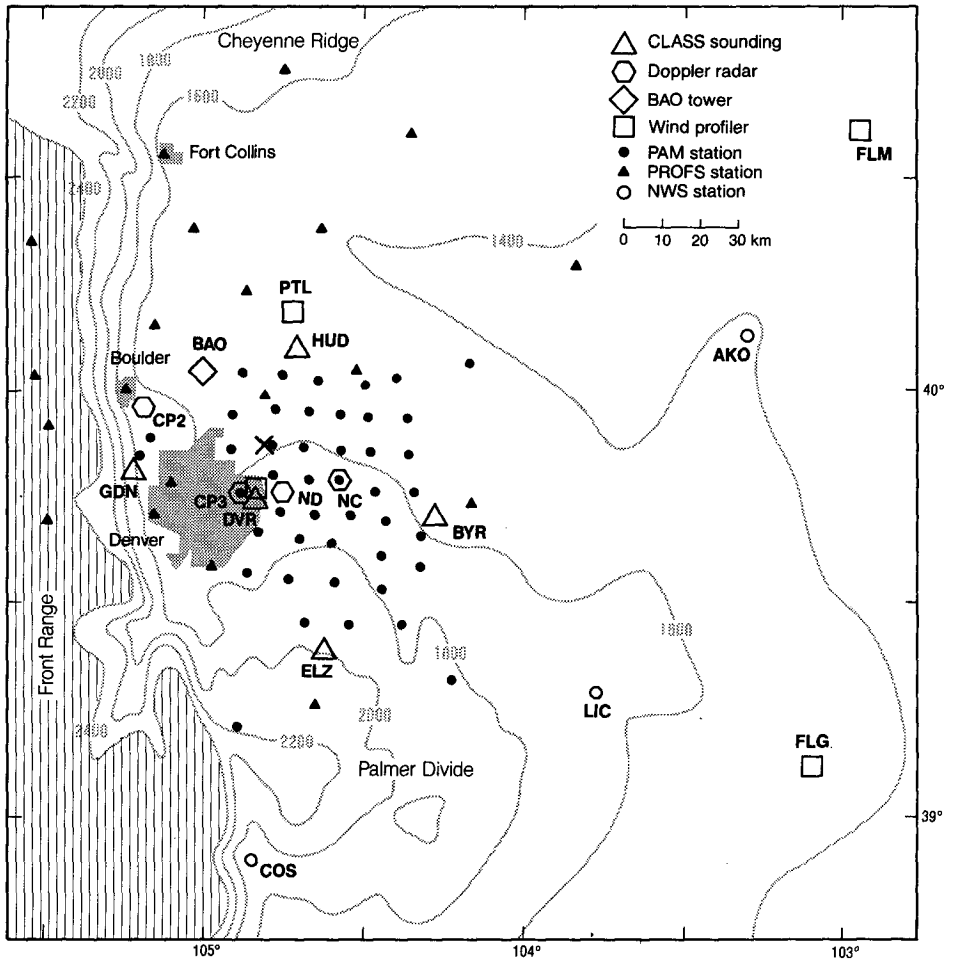

FIG. 1. Topographic map of the CINDE area, showing instrument locations. The elevation contour interval is 200 m, and elevations greater than 2400 m are hatched. Wind profilers were located at Fleming (FLM), Flagler (FLG), Platteville (PTL), and Denver (DVR). CLASS soundings were taken at Byers (BYR), Denver (DVR), Elizabeth (ELZ), Golden (GDN), and Hudson (HUD). The Doppler radars were NOAA-C (NC), NOAA-D (ND), NCAR CP-3, and NCAR CP-2. National Weather Service stations were at Akron (AKO), Limon (LIC), and Colorado Springs (COS). The tornado occurred 15 km north-northeast of the CP-3 radar and is marked by the ×. The cities of Denver, Boulder, and Fort Collins are shaded.

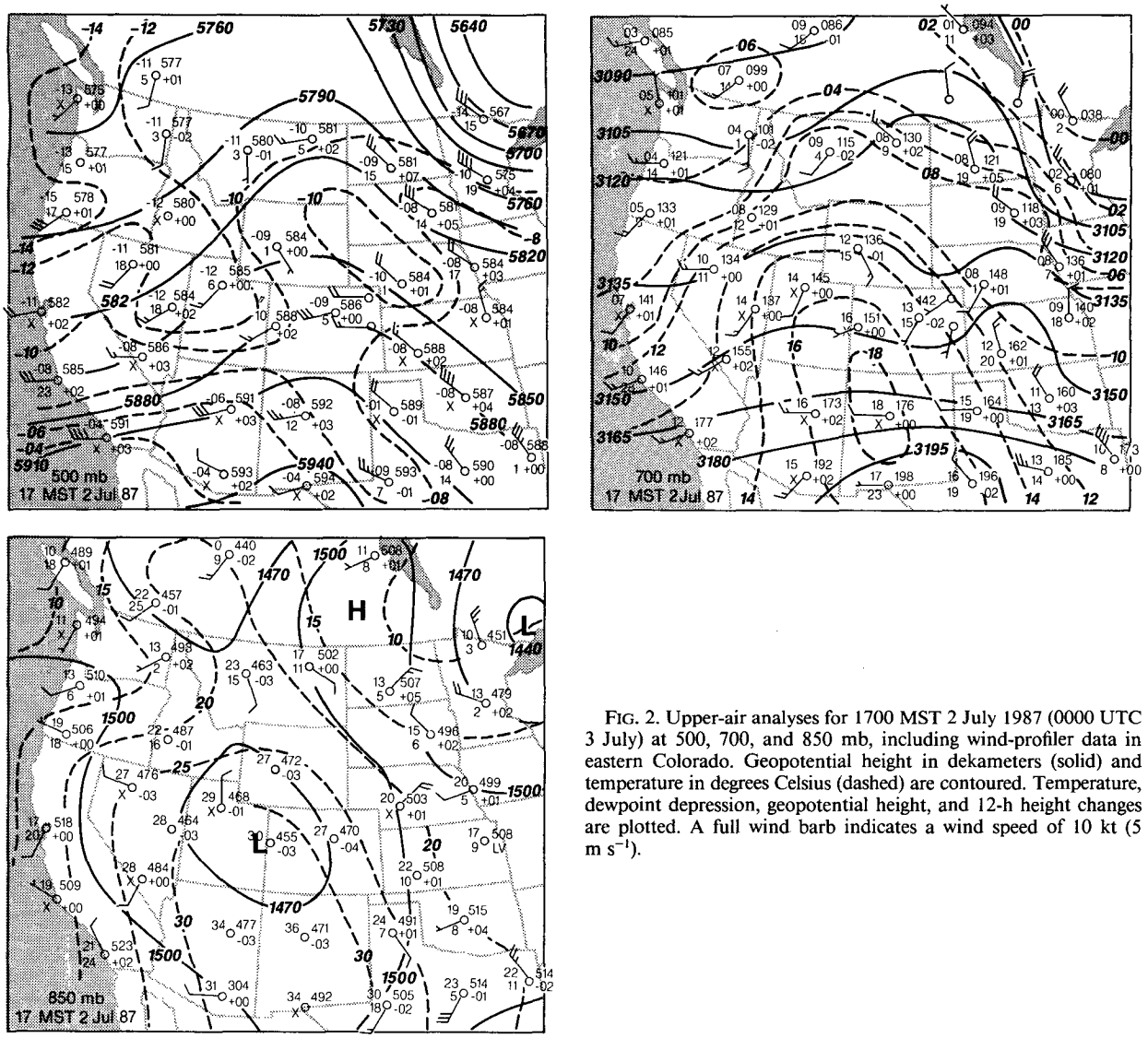

FIG. 2. Upper-air analyses for 1700 MST 2 July 1987 (0000 UTC 3 July) at 500, 700, and 850 mb, including wind-profiler data in eastern Colorado. Geopotential height in dekameters (solid) and temperature in degrees Celsius (dashed) are contoured. Temperature, dewpoint depression, geopotential height, and 12-h height changes are plotted. A full wind barb indicates a wind speed of 10 kt (5 m s^{-1}).

(NOAA), the National Center for Atmospheric Research (NCAR), and several universities. Instrumentation used in the present analysis includes 4 NOAA wind profilers, 22 NOAA Program for Regional Observing and Forecasting Services (PROFS) and 45 NCAR Portable Automated Mesonet (PAM) surface stations, 5 Cross-chain Loran Atmospheric Sounding Systems (CLASS), 3 mobile balloon sounding systems, and the NCAR CP-3, CP-2, NOAA-C (NC), and the NOAA-D (ND) radars. The instrument locations, major cities, and topography of the experimental area are shown in Fig. 1. Additional details on the CINDE project are given by Wilson et al. (1988).

An important feature of the mesoscale environment on 2 July was the development of an ~70-km diameter topographically forced vortex known as the Denver Cyclone. Denver cyclones have been associated with the development of severe weather (Blanchard and Howard 1986; Wilczak and Glendening 1988; Wilczak and Christian 1990) and especially with the formation of tornadoes (Szoke et al. 1984; Dunn 1990). In particular, using 10 years of observations, Szoke and Augustine (1990) have shown that a very high statistical correlation exists between the occurrence of tornadoes and the Denver Cyclone. Indeed, the nonsupercell tornado studied by Brady and Szoke (1989), and several of the stronger tornado vortices discussed by WW89, occurred within Denver cyclones.

The 2 July tornado, together with several weaker vortices, developed along a stationary convergence boundary that was embedded within the Denver Cyclone flow. The tornado formed under a rapidly growing convective cell that was part of a line of multicellular convection and remained a visible funnel for 17

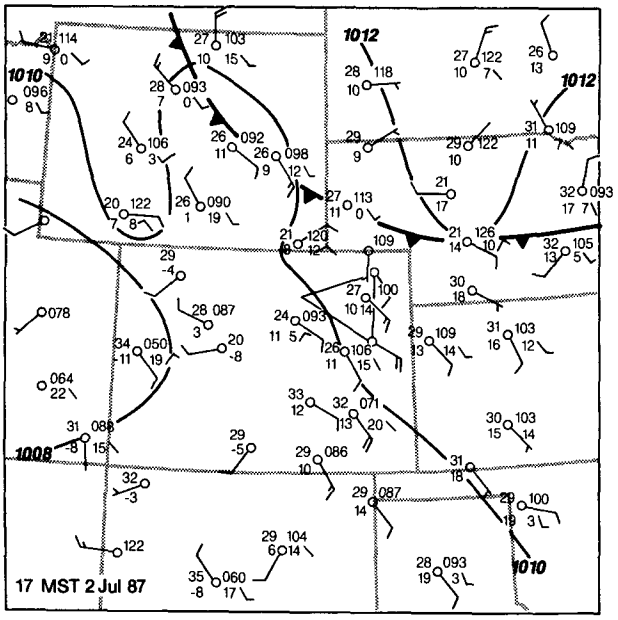

FIG. 3. Surface analysis for 1700 MST 2 July 1987 (0000 UTC 3 July), with a contour interval of 2 mb. Temperature (°C), dewpoint temperature (°C), pressure (mb), and 3-h pressure tendencies are plotted. The location of the profiler triangle is also shown. A full wind barb indicates a wind speed of 10 kt (5 m s^{-1}).

min, between 1424 and 1441 MST. Through a time–height analysis of maximum horizontal shear derived from a single Doppler radar, WW89 demonstrated that the tornado-associated vertical vorticity developed within the lowest 2 km, without a preceding midlevel mesocyclone. Based on an analysis of tornado debris, they estimated that the tornado reached high F1–low F2 intensity (Fujita 1981).

The present analysis of the 2 July tornado addresses two issues. The first is to document the larger-scale environment preceding tornadogenesis in sufficient detail to aid in the forecasting of this type of tornado. Second, we investigate mechanisms and processes that contribute to vorticity generation down to the tornado parent vortex scale. The pretornadic environment is described, and the role of the Denver Cyclone in contributing to tornadogenesis is evaluated. Next, vorticity budget terms are calculated in the immediate tornado environment and are compared to similar observations within supercell tornadic storms. Finally, the proposed mechanism for nonsupercell tornadogenesis is evaluated in light of the current observations.

A limitation of the vorticity analysis is the coarse (500-m) resolution of the radar data used in its calculation. This restricts the analysis to the tornado's parent vortex circulation rather than to the tornado itself, and also precludes an analysis at heights in the dynamically important region below 1 km.

Companion papers to this study focus on detailed features of the tornado vortex, made possible by special high-resolution NOAA-C and NOAA-D scans, implemented after the tornado was in its mature, visible stage. These papers include a combined photogrammetric and Doppler radar analysis (Part II, Wakimoto and Martner 1992), and a study of the finescale, three-dimensional reflectivity and velocity structure in the immediate tornado vicinity (Part III, in progress).

2. Synoptic setting

Upper-air analyses at 500, 700, and 850 mb for 1700 MST 2 July (0000 UTC 3 July), including wind-profiler data in eastern Colorado, are presented in Fig. 2. The synoptic pattern at 500 mb displays typical midsummer characteristics, with the jet stream generally near the Canadian border and a ridge over the Rocky Mountain region. Winds aloft at Denver were west-southwest at 15 m s^{-1}. At 700 and 850 mb, a ridge, located along the Front Range of the Rocky Mountains 12 h earlier at 0500 MST 2 July (1200 UTC 2 July), was now over central Nebraska and Kansas. A 700-mb short-wave trough, present over Utah 12 h earlier, had amplified and was now located in eastern Colorado. The 850-mb heights to the west had fallen throughout the day, forming a closed low over Utah and western Colorado. As a result of the falling pressures to the west, rising pressures to the east, and the consequent development of diurnal upslope flow over the sloping plains, surface winds in eastern Colorado were southeasterly at 1700 MST (Fig. 3). Surface dewpoint temperatures ranged from 10° to 13°C throughout the day.

The forcing associated with the passage of the synoptic ridge and approaching short-wave trough were assessed using quasigeostrophic (QG) diagnostics

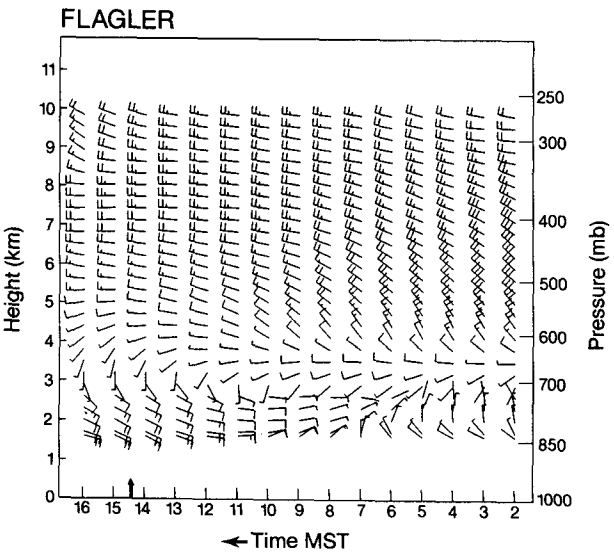

FIG. 4. Time–height analysis of profiler winds from Flagler (FLG). The surface elevation is 1463 m MSL. The vertical arrow at 1420 MST indicates the time of tornado formation.

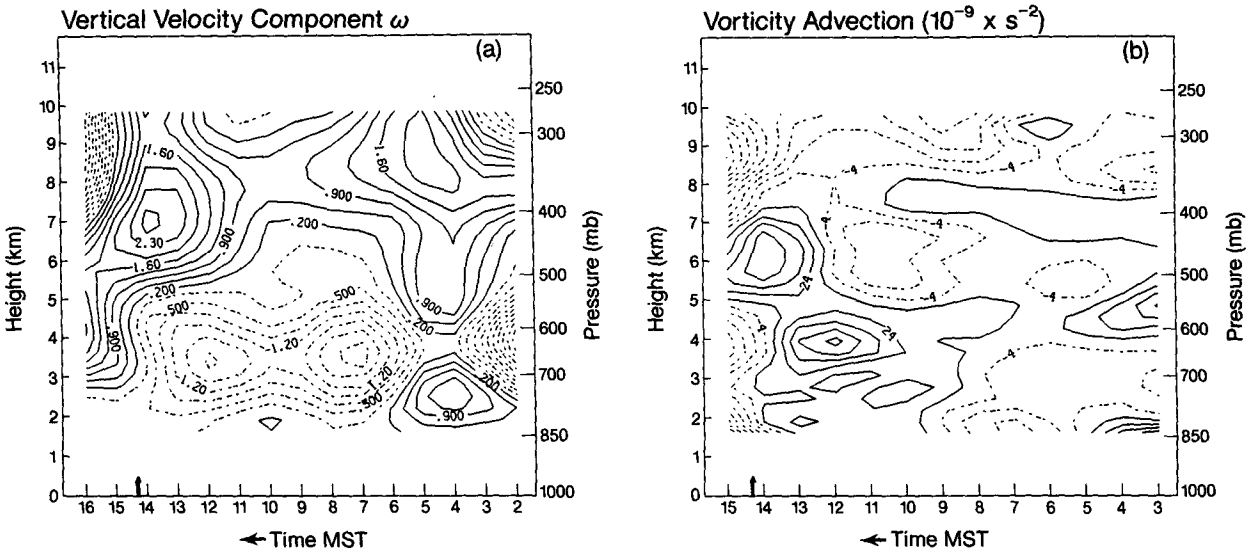

FIG. 5. Time–height analyses (km MSL) from the triangle of profilers at FLM, FLG, and PTL on 2 July 1987: (a) vertical velocities, with a contour interval of 0.35 μb s^{-1}, and (b) vorticity advection, with a contour interval of 14 × 10^{-9} s^{-2}. Dashed lines indicate negative contours. The vertical arrow at 1420 MST indicates the time of tornado formation.

(Hoskins and Pedder 1980). Applying the method of calculation of Barnes (1985) to the standard upper-air data, we find that at 0500 MST the divergences of the **Q**-vector fields at 600 and 800 mb were small and negative ($\sim -2 \times 10^{-17}$ s^{-3} mb^{-1}) over Colorado, indicative of weak upward vertical motion. The QG diagnostics alone gave little indication of the potential for severe convection later that afternoon; however, because of the coarse spatial resolution of the standard upper-air data used in the QG analysis, the actual forcing associated with the short-wave feature is likely to be significantly underestimated. To determine the short-wave forcing, observations made with the radar wind-profiler network were utilized.

3. Wind-profiler observations

Subsynoptic-scale forcing was calculated using wind profiles from 50-MHz radar profilers at Platteville and Flagler, Colorado, and from a 405-MHz profiler at Fleming, Colorado (Fig. 1), using the method of Zamora et al. (1987). The three profilers form an equilateral triangle ~ 150 km on a side. The lowest range gate of the 50-MHz radars is 1500 m AGL. At the Flagler site, winds below 1500 m were obtained with a Doppler sodar, which provided data from the surface up to 600 m; above this the winds were interpolated to 1500 m. At Platteville, the low-level winds were linearly interpolated between a surface measurement and the lowest profiler level. The 405-MHz profiler at Fleming provided winds down to 500 m. Below this the winds were also linearly interpolated to a surface measurement. All winds were smoothed with a two-pass Von Hann filter.

At Flagler (Fig. 4), the low-level winds turned easterly near 0800 MST, in response to the developing 850-mb low pressure over the mountains and to heating over the sloping plains, and continued to strengthen and deepen with time. In addition, the passage of the ridge near 600–700 mb is evident at 1300 MST.

An estimate of vertical motion was calculated through vertical integration of the divergence field derived from the profiler-triangle winds (Fig. 5a). After 0600 MST the vertical velocity field shows destabilizing upward motion below 500 mb, with a local maximum of -1.9 μb s^{-1} at 650 mb at 1200 MST. Associated with this upward vertical motion was a period of positive vertical vorticity advection (Fig. 5b) between 0900 and 1400 MST that extended from the surface to ~500 mb. After ~1400 MST the wind-profiler data were influenced by developing convection.

The destabilizing effect of the short-wave trough is expected to have begun shortly after passage of the preceding ridge axis (Holton 1979). Wind-profiler data taken every 12 min by the profiler operating at the Denver (DVR) site clearly show passage of the ridge axis at 1100 MST at 600 mb (Fig. 6). In comparison, the ridge axis was observed to pass the Flagler profiler, which was 140 km farther east, at 1300 MST. Finally, balloon sounding observations taken at the DVR profiler site show that the developing southeasterly flow was limited to the depth of the growing convective boundary layer, as indicated in Fig. 6.

4. Preconvective environment (0500–1300 MST)

The dominant mesoscale feature occurring on 2 July was the development of the ~70-km diameter, oro-

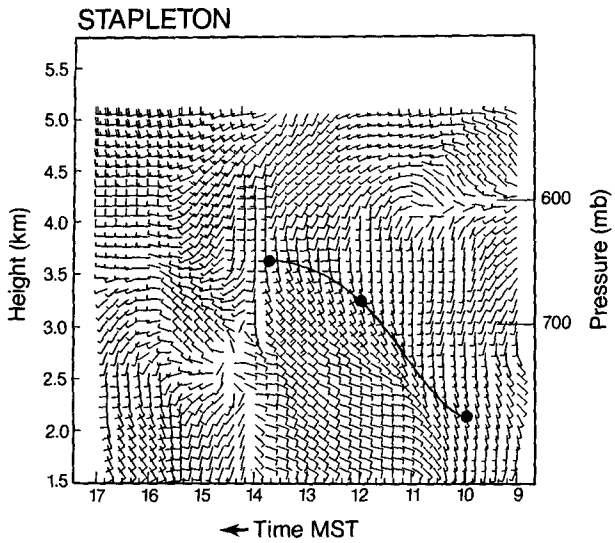

FIG. 6. Time–height cross sections from the Denver Stapleton profiler of filtered horizontal winds sampled every 12 min, and the boundary-layer height (solid line), determined by DVR soundings at 1000, 1200, and 1345 MST. Heights are kilometers (MSL).

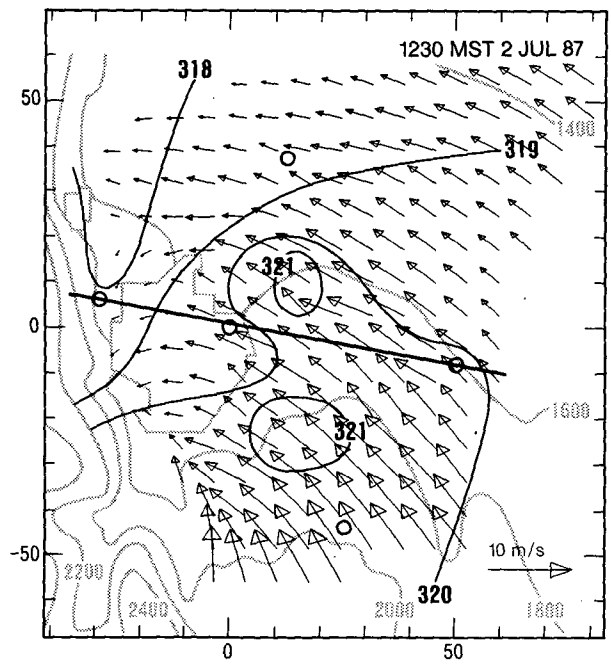

FIG. 7. Gridded surface winds and virtual potential temperatures (K, dark contour lines) from hourly averaged data centered at 1230 MST. Terrain contours are shown (plotted every 200 m) and the cities of Denver and Boulder are outlined in gray. Circles indicate the five CLASS sites. The origin is Stapleton International Airport, where the CP-3 radar, the 915-MHz radar wind profiler, and the Denver CLASS sounding site were located. Axis coordinates are kilometers from CP-3. The heavy solid line indicates the orientation of the sounding cross section of Fig. 9a.

graphically forced Denver Cyclone (DC). The vortex frequently forms in response to southeasterly winds flowing over the Palmer Divide (Fig.1), an ~800-m ridge located on the southern edge of the CINDE network (Wilczak and Christian 1990).

The development of the DC on 2 July is traced through the surface mesonet wind, thermodynamic, and pressure fields (bias corrections incorporated into the PAM thermodynamic data are discussed in appendix A). Between 0730 and 1030 MST winds in the surface network became southeasterly as the 850-mb low developed over the mountains to the west. At 1230 MST (Fig. 7), the first signs of an incipient DC became apparent, manifest as a region of weaker flow and corresponding low-level convergence near Denver, with very weak northeasterly flow developing along the foothills to the west of Denver. The surface virtual potential temperature θ_v pattern shows a warm plume developing east of Denver in the lee of the Palmer Divide with cooler temperatures along the foothills, a pattern that is characteristic of DC formation (Wilczak and Glendening 1988; Szoke 1991).

At 1200 MST, CLASS soundings were taken at Golden (GDN), DVR, and Byers (BYR). Comparing the 1200 MST DVR sounding with the 0500 MST DVR sounding (Fig. 8), we see that a well-mixed convective boundary layer had grown to 700 mb. This layer was capped by a strong temperature inversion and sharp moisture gradient, above which was a second, deep, thermodynamically well-mixed layer extending to ~530 mb. Winds in the upper mixed layer had a westerly component, and the temperature within this second layer was ~2°C warmer than in the 0500 MST

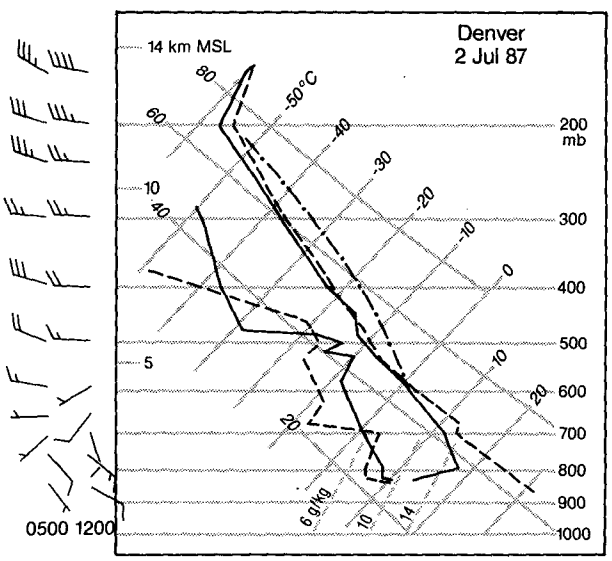

FIG. 8. The Denver skew T–log$p$ sounding at 0500 MST (solid) and Denver CLASS sounding at 1200 MST (dashed).

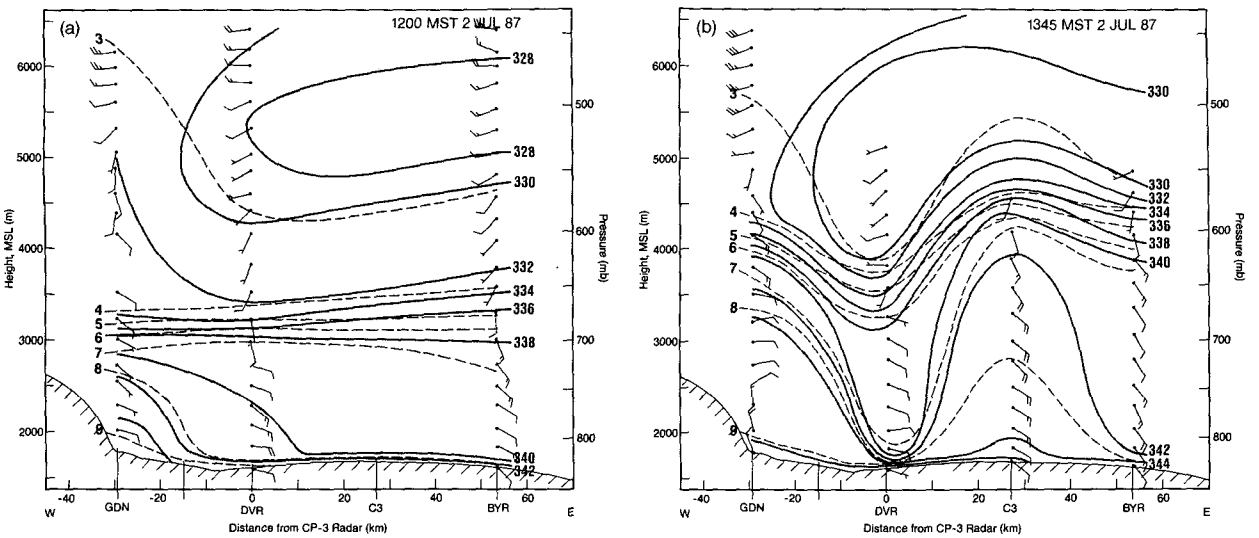

FIG. 9. West–east cross sections of winds, equivalent potential temperature (K, solid lines), and mixing ratio (g kg^{-1}, dashed lines) at (a) 1200 MST (constructed from soundings at GDN, DVR, and BYR) and (b) 1345 MST (constructed from soundings at GDN, DVR, C-3-NC, and BYR).

sounding. These characteristics suggest that this upper layer was a convectively mixed boundary layer that developed over the higher mountainous terrain to the west, and advected eastward, overriding the plains' boundary layer (Carlson et al. 1983; Benjamin and Carlson 1986). The primary effect of the mountain boundary layer was to increase the strength of the 700-mb inversion through differential advection, thereby increasing the convective temperature, and delaying the onset of convection. Using the lowest 50-mb average mixing ratio from the 1200 MST sounding, we find a convective available potential energy (CAPE) value of ~772 J kg^{-1}.

A west–east cross section of equivalent potential temperature θ_e, moisture q, and winds was constructed from the 1200 MST soundings at GDN, DVR, and BYR, with an orientation as indicated in Fig. 7. The cross section (Fig. 9a) reveals a nearly uniform, lower well-mixed plains convective boundary layer ~ 1500 m deep. A strong capping inversion at the top of the plains' mixed layer sloped downward toward the west, with the winds veering to a more southwesterly direction aloft.

5. Convective development (1300–1440 MST)

a. Mesoscale features

Mesonet wind and boundary-layer reflectivity fields at 1340 MST are shown in Fig. 10a. Numerous longitudinally oriented bands of clear-air reflectivity greater than 5 dBZ were present with a spacing and orientation suggesting that they were associated with boundary-layer roll vortices (Lemone 1976). The largest band passed through the center of the CINDE network and then curved to the southwest in response to the evolving Denver Cyclone, which had developed strong northerly flow to the north and west of Denver.

At this time a weak gust front (boundary A in Fig. 10a), visible in the surface mesonet and low-level CP-3 data, had propagated into the CINDE network from the north, where it originated as an outflow from a thunderstorm located ~30 km west of Fort Collins at 1200 MST.[1] In addition, a stationary convergence zone (boundary B) separating northerly and southeasterly flow had developed to the south of the cyclone center. This stationary boundary is a common feature of the Denver Cyclone (Szoke et al. 1984) and is commonly referred to as the Denver Cyclone convergence and vorticity zone (DCVZ).

A third, nearly stationary boundary (labeled C in Fig. 10a) was evident in the low-level CP-3 velocity data as a narrow zone of convergence. This convergence boundary was associated with the largest of the bands of enhanced reflectivity. The location and orientation of boundary C appears to have been related to the local topography, ambient southeasterly flow, and evolving Denver Cyclone. Enhanced convergence along a similarly located and oriented line was also observed in the DC case study of Wilczak and Christian (1990),

[1] Boundaries are defined as thin lines of enhanced reflectivity and/or convergence in Doppler velocity following Wilson and Schreiber (1986).

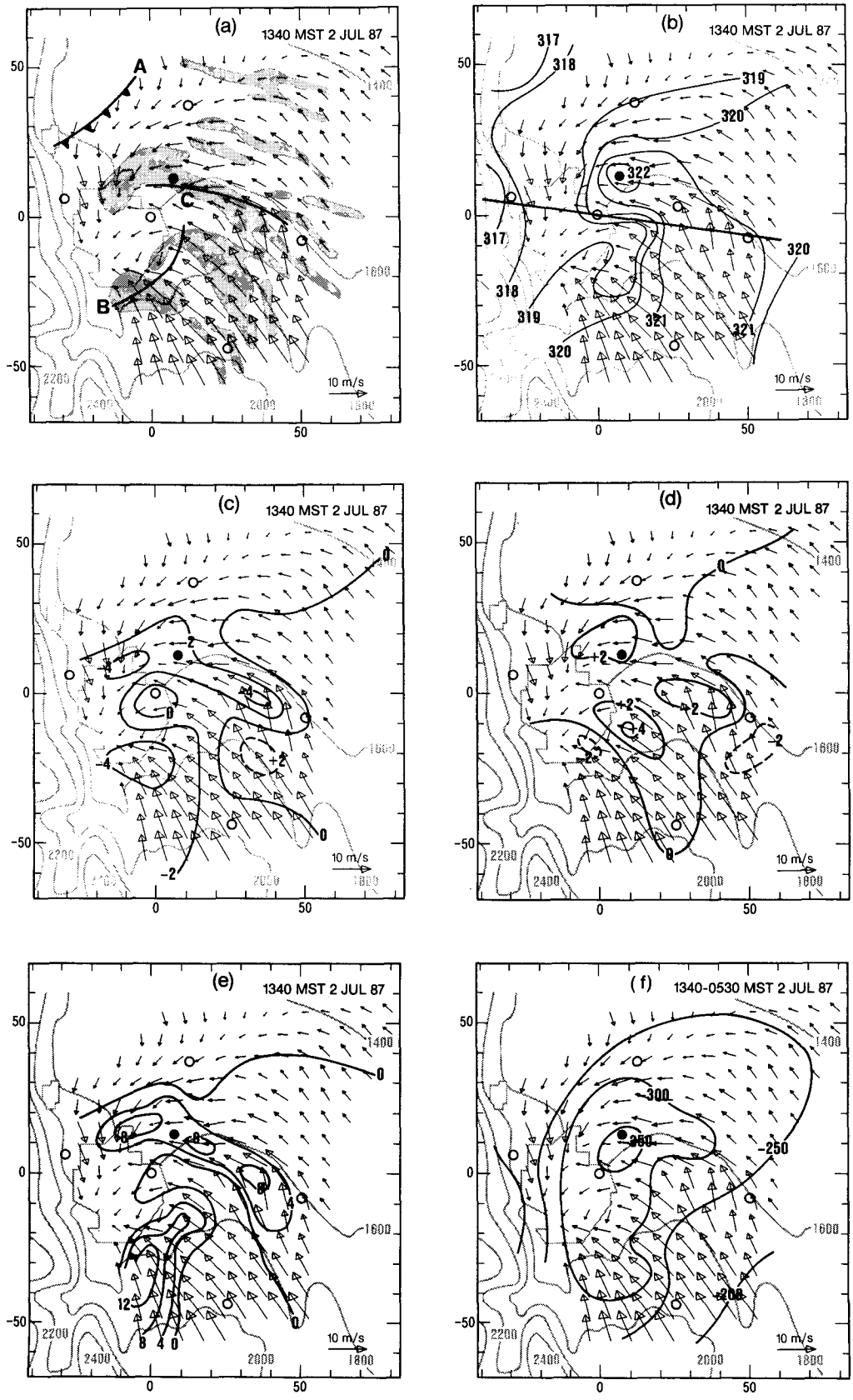

suggesting that this boundary may be a relatively common feature of the Denver Cyclone.

The difference in temperature between the warm plume on the east side of the DC and the cooler region near the foothills had increased at 1340 MST, with temperature gradients reaching 3°C (10 km)$^{-1}$ near the cyclone center (Fig. 10b). The highest θ_v was ~15 km northeast of CP-3, near where the tornado would form ~40 min later. The moisture field (not shown) indicates mixing ratios of ~8.5 g kg^{-1} with little variability, except for 1–2 g kg^{-1} higher values at the mesonet stations bordering the foothills, and for high values to the northwest associated with thunderstorm outflow boundary A.

The surface wind divergence field at 1340 MST (Fig. 10c) shows a northwest–southeast-oriented band of convergence coincident with boundary C, and a strongly convergent region to the south near the DCVZ (boundary B). Near the cyclone center [$(x, y) \approx (0, 0)$ km] the surface winds were divergent. The relative vertical-vorticity field indicates a broad region of positive vorticity associated with the DC, with several pockets of high vorticity embedded within (Fig. 10d). Using the surface vorticity and divergence fields, the time rate of change of vorticity due to stretching was calculated. This term was positive near the DCVZ (Fig. 10e), and also along boundary C, where it reached maximum values of 8×10^{-8} s^{-2}. If the convergence were constant with time in the tornado development region ($\sim 3 \times 10^{-4}$ s^{-1}) between 1340 and 1420 MST, stretching would increase the relative vorticity from 2×10^{-4} s^{-1} to only 5.2×10^{-4} s^{-1}.

The change in surface pressure between 0530 MST (when the surface winds were uniformly southwesterly) and 1340 MST indicates the pressures had been falling throughout the CINDE network (Fig. 10f). Larger pressure falls occurred within the area of the DC, with the maximum pressure fall in the region where the tornado formed ~40 min later. This was also the location of the warmest surface θ_v (Fig 10b). The relative change in pressure within the DC relative to its surrounding environment was ~1.5 mb. A qualitatively similar pressure change field was found using a 3-h interval preceding 1340 MST.

At ~1345 MST, balloon soundings were taken at the GDN, DVR, and Hudson (HUD) CLASS sites, and at two mobile locations: C-2 at $(x, y) = (-10.8, 31.9)$ km and C-3 at the NC radar site $(x, y) = (27.6, 2.5)$ km. Approximately 25 min later, at 1411 MST, a sounding was taken at BYR. Using GDN, DVR, C-3, and BYR, a west–east cross section was drawn through the center of the DC, with an orientation as indicated in Fig. 10b.[2]

The cross section at 1345 MST (Fig. 9b) was considerably more disturbed than at 1200 MST, due in part to the presence of the DC and in part to the presence of clouds at that time. The cross section shows brisk well-mixed southeasterly winds at BYR and C-3; lighter, more easterly winds at DVR; and low-level northerlies at GDN with velocities exceeding 10 m s^{-1}.

In comparison with the 1200 MST cross section, the 1345 MST cross section shows that boundary-layer depths had increased by over 800 m except at DVR. Mixing ratios in the lowest 500 m had on average increased slightly from 1200 MST to values averaging 7.8 g kg^{-1}, with a somewhat higher value (8.2 g kg^{-1}) at C-3 and considerably lower value (7.0 g kg^{-1}) at DVR[2]. The lower moisture and shallower boundary-layer depth at DVR suggests sinking motion, which is consistent with the divergent surface winds pattern (Fig. 10a,c). [Wilczak and Christian (1990) also observed a similar divergent surface wind pattern, and they and Szoke (1991) observed a distinct cloud-free region in the center of the DC, all indicating subsidence near the cyclone center.] The deepest boundary-layer (2700 m) was measured at C-3, which was near the stationary convergence boundary C. Although the surface mesonet data indicate nearly uniform surface moisture throughout the region, the C-3 sounding shows that the high surface moisture extended upward through the lowest 1000 m at C-3, but only 20–30 m at DVR and BYR. It appears that the deeper moisture near boundary C resulted from low-level moisture convergence associated with the boundary. [A deeper boundary layer and higher moisture values were also observed along a DC boundary in the study of Szoke and Brady (1989).]

A comparison of the ~1345 MST soundings at GDN, DVR, and HUD with soundings at the same locations at ~1200 MST reveals an ~1°–2°C cooling in the layer between the top of the convective boundary layer and the 500-mb level. This cooling is consistent with the approach of the 700-mb short-wave disturbance and was responsible for an erosion of the strong temperature inversion capping the PBL that had developed due to the advected mountain boundary layer aloft.

[2] Because of an observed systematic error in the mobile sounding relative humidities, corrections were applied to these soundings (see appendix B).

FIG. 10. Gridded surface mesonet winds for the 5-min period ending at 1340 MST, shown with (a) areas having boundary-layer clear-air reflectivities greater than 5 dBZ shaded, and boundaries A, B, and C; (b) contours of virtual potential temperature (K); (c) contours of surface mesonet divergence with a contour interval of 2×10^{-4} s^{-1}; (d) contours of relative vorticity with a contour interval of 2×10^{-4} s^{-1}; (e) contours of the stretching term with a contour interval of 4×10^{-8} s^{-2}; and (f) contours of pressure change (Pa), with a contour interval of 50 Pa, between 0530 and 1340 MST. Open circles denote sounding locations, and the heavy solid line in (b) indicates the orientation of the sounding cross section of Fig. 9b. The solid circle at $(x, y) = (6, 12)$ km marks where the tornado formed ~40 min later.

Values of CAPE were calculated for each sounding using near-surface 50-mb averages of mixing ratio and potential temperature. However, only two soundings, DVR and HUD, were tracked well above the tropopause; the remaining soundings were terminated in the middle to upper troposphere so that additional soundings could be released. To calculate CAPE values for each sounding, the average of the DVR and HUD soundings were used as proxy data at upper levels. Because the greatest thermodynamic variability is expected at lower levels, the use of upper-level proxy data is unlikely to have significantly influenced the CAPE calculations.

Of the six soundings, DVR, HUD, and C-2 had very low CAPE values of 493, 326, and 236 J kg^{-1}, respectively (Table 1). The BYR sounding had a moderate CAPE value of 645 J kg^{-1}, while GDN and C-3 had the highest CAPE values, 1064 and 1173 J kg^{-1}, respectively. The BYR and C-3 soundings had higher CAPE values in part because of the higher near-surface temperatures associated with the plume of warmer air on the east side of the DC (Fig. 10b). In contrast, DVR, HUD, and C-2 were in the region of cooler surface temperatures. Additionally, GDN and C-3 had higher CAPE values because of their higher lowest 50-mb moisture values. The highest CAPE, at C-3, resulted from warmer surface temperatures and the moisture convergence occurring along boundary C.

Values of CAPE and lifted index (LI) are listed in Table 1. Although a large variability exists due to the presence of the DC and related convergence boundaries, four of the six soundings have values typical of High Plains severe weather. For example, Fankhauser and Wade (1982) found an average CAPE of 520 J kg^{-1} and a LI of −3.0°C for 57 hail days during the National Hail Research Experiment.

Wind hodographs for the GDN, DVR, and BYR soundings are shown in Fig. 11. The three hodographs are similar above ~4 km MSL; below this they vary significantly because of the low-level Denver Cyclone flow. In general the hodographs have a directional shear similar to the mean hodographs for tornadic thunderstorms derived by Maddox (1976). The 2 July hodographs differ, however, in that their upper-level winds are only approximately half as strong as those found in the Maddox study.

TABLE 1. CAPE and lifted index for tornado proximity soundings.

Location	Time (MST)	CAPE (J kg^{-1})	LI (°C)
DVR	1343	493	−2.73
HUD	1349	326	−0.94
BYR	1411	645	−3.57
GDN	1351	1064	−4.32
C-3 (NOAA-C)	1335	1173	−5.53
C-2 (BAO)	1335	236	−2.00

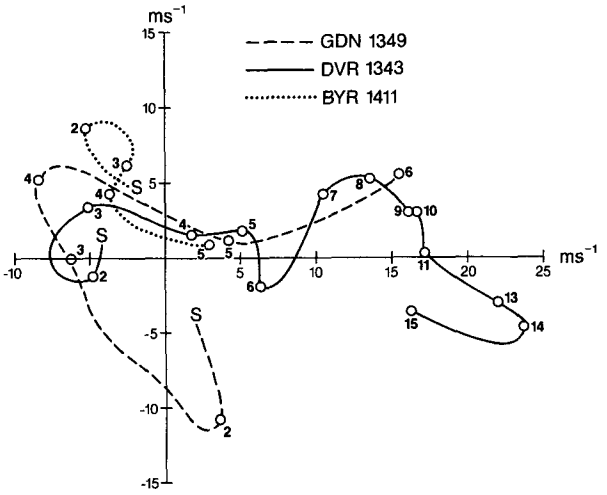

FIG. 11. Wind hodographs from the GDN, DVR, and BYR soundings at the times indicated. The S marks the surface, and the numbers indicate altitude (km MSL).

Because of its high correlation with supercell and mesocyclone generation, storm-relative helicity has been proposed as an indicator of tornado potential (Davies-Jones et al. 1990; Lazarus and Droegemeier 1990). Helicity calculated relative to the propagation of the tornado parent vortex (see section 5b) for the layer from 0–3 km AGL is only approximately 30 $m^2 s^{-2}$ for the 1343 MST Denver sounding and 110 $m^2 s^{-2}$ for the 1335 MST C-3 sounding. In comparison, Davies-Jones suggests that higher helicity values, in the range 150–300 $m^2 s^{-2}$, are required for weak tornadoes (F0–F1) associated with supercell mesocyclones.

b. Storm-scale features

The evolution of boundaries A, B, and C of Fig. 10a, as seen in the surface mesonet and low-level CP-3 velocity data, is traced in Fig. 12. At 1310 MST (not shown) boundary C extended nearly 20 km to the northwest of CP-3. By 1350 MST the northeasterly flow of the DC intensified considerably; as it did, convergence along boundary C intensified, and the western portion of boundary C shifted significantly toward the south, forming a bend (Fig. 12a). At this time the convergence boundary also became considerably more convoluted in the vicinity of surface mesonet station PAM13. Associated with each fold in the boundary were local azimuthal shear maxima, detected in the low-level CP-3 velocity data. A region of weak reflectivity (~10 dBZ) was located just upwind (east) of the bend in boundary C. In addition, multicellular convection had begun to develop to the north of boundary C. Finally, a north–south-oriented zone of weak near-surface convergence, related to the rapidly developing DC, had formed ~5 km northwest of PAM13, indicated as boundary D.

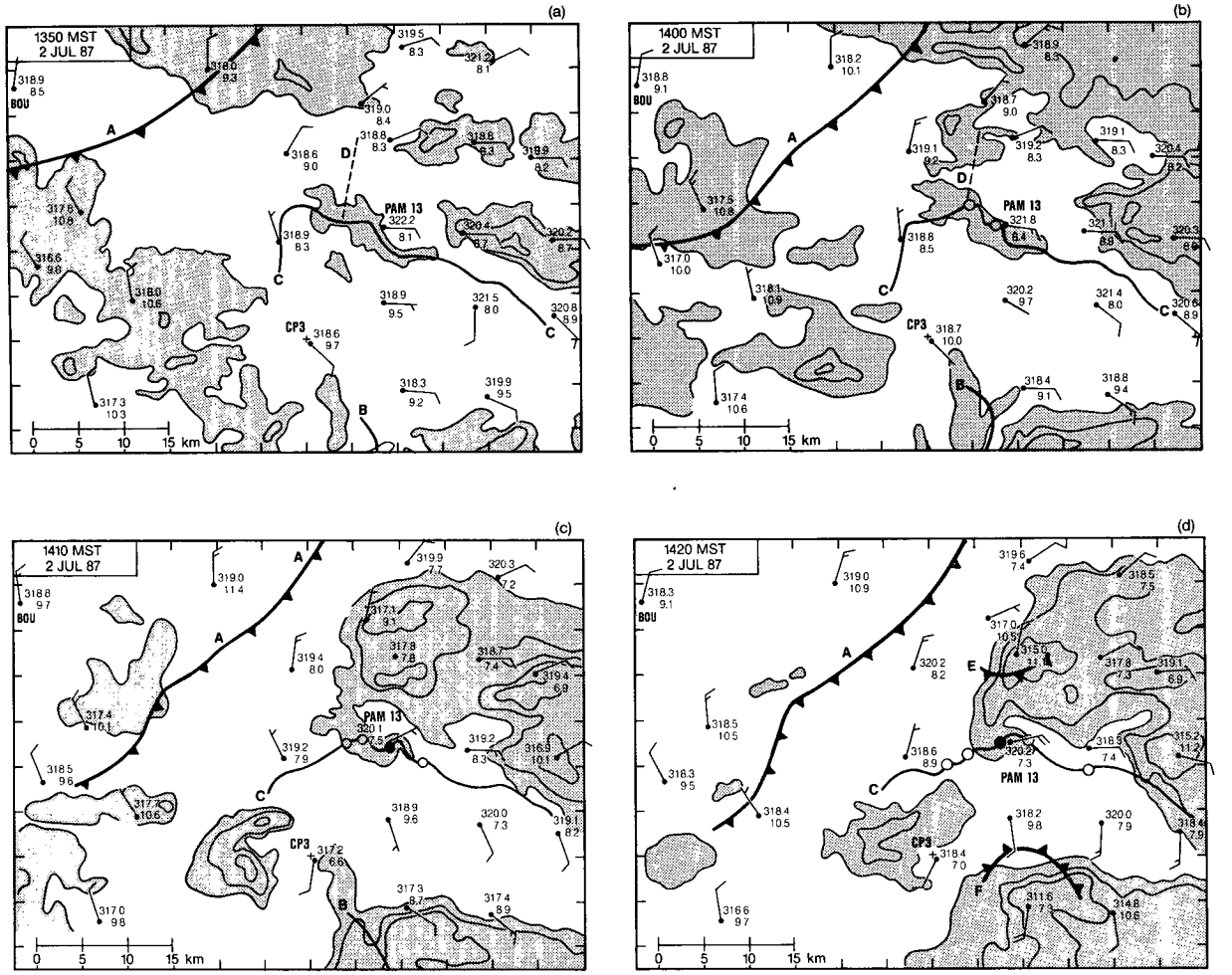

FIG. 12. The evolution of low-level convergence boundaries (labeled A–F) for the time interval between 1350 and 1420 MST 2 July 1987. Also shown are surface wind (full barb = 5 m s^{-1}), virtual potential temperature (K), and mixing ratio (g kg^{-1}) from PROFS and PAM mesonet stations. Reflectivity from the CP-3 radar, at a 7.5° elevation, is plotted with contours of 10, 30, and 50 dBZ. The location of the CP-3 radar is indicated. On boundary C, open circles denote vorticity maxima, and the closed circle is the tornado parent vortex.

Between 1350 and 1400 MST, the azimuthal shear maxima on the boundary (denoted by open circles in Fig. 12b) had strengthened and were slowly propagating to the northwest. The convection to the north of boundary C grew southward toward boundary C preferentially along the low-level convergence of line D.

Between 1400 and 1410 MST the convection to the north of boundary C intensified and developed two distinct cells with reflectivity greater than 50 dBZ (Fig. 12c). The cell nearest PAM13 developed new growth on its southern edge and became continuous with the enhanced reflectivity along boundary C, forming a hooklike structure. The bridge connecting these two initially distinct regions of enhanced reflectivity appears to have formed along the weak convergence line D. At this time the incipient tornado parent vortex (denoted as a solid circle on boundary C; referred to as vortex C2 in WW89) had advected under the easternmost extremity of the hooklike echo, where it created a small indentation of low reflectivity in the hook.

Single-Doppler radar velocity scans show that between 1400 and 1420 MST the tornado parent vortex slowly propagated to the northwest (321°) at a speed of 2.3 m s^{-1}. At 1420 MST the tornado parent vortex, which was just becoming visible as a dust whirl on the ground, was situated under the center of the hooklike echo (Fig. 12d). The two shear maxima to the west of the tornado propagated to the edge and beyond the hook. Meanwhile, new vortices developed and strengthened to the east of the tornado vortex. Between 1400 and 1420 MST, boundary A propagated little, moving only to within 17 km of the tornado, and had no apparent effect on tornadogenesis.

By 1420 MST, two new outflow boundaries had become apparent in the mesonet and radar velocity data (Fig. 12d). The propagation of these boundaries (E and

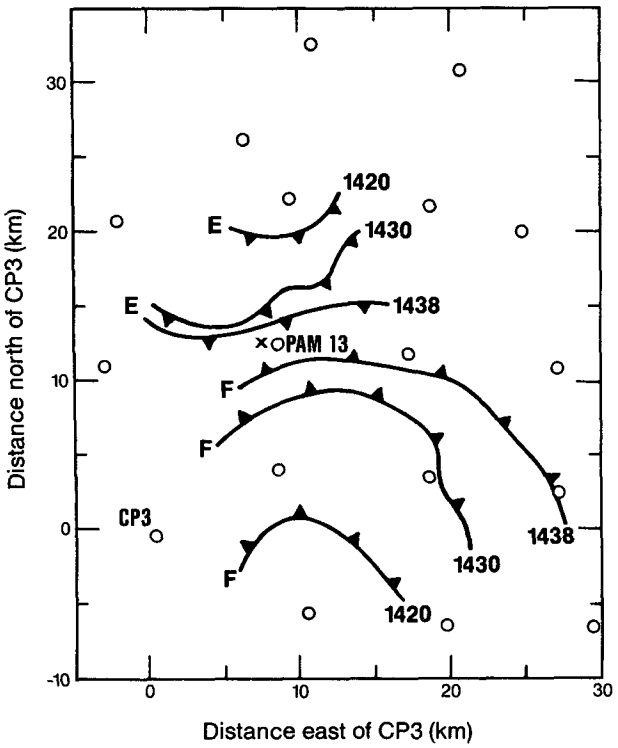

FIG. 13. Isochrones of outflow boundaries E and F at 1420, 1430, and 1438 MST 2 July 1987. Open circles denote surface mesonet locations. The × marks the location of the tornado at 1424 MST.

F) is displayed in Fig. 13 at 1420, 1430, and 1438 MST. The first of these, boundary E, developed from the cell north of PAM13; it passed the mesonet station located 9.7 km north of PAM13 at ~1415 MST with a temperature drop of 4°C, a mixing ratio increase of 3 g kg^{-1}, and a 2 m s^{-1} speed increase with the direction shifting from 30° to 350° over a 10-min period. The second outflow (boundary F) developed from a cell to the south that formed on the DCVZ. This boundary passed the mesonet station south of PAM13 at 1428 MST, where over a 10-min period the temperature dropped 3°C, the mixing ratio dropped by 3 g kg^{-1}, and the wind speed increased from 5.5 to 18.5 m s^{-1} while the direction stayed constant at 170°.

Boundaries E and F converged on the tornado from opposite directions. The effect of these two boundaries on the formation of the tornado does not appear to have been significant, considering that at 1424 MST, when the tornado had just become visible, the two boundaries were more than 6 km from the tornado. From the analysis of Part II it appears that after ~1437 MST, cold air from outflow E collided with the base of the tornado, thereby contributing to the tornado's demise. This was followed shortly afterward by boundary F propagating into the area. The evolution of the tornado, and its interaction with outflow boundary E, can be seen in a time series of photographs presented in Wilson et al. (1988).

Following the dissipation of the tornado, its parent storm propagated to the east (at 80°), intensified to greater than 70 dBZ, and developed significant cyclonic rotation. This cell coalesced with cells originating along the DCVZ, forming a north–south-oriented squall line that continued to propagate eastward, eventually dissipating in central Oklahoma more than 24 h later.

6. Multiple-Doppler radar vorticity analysis

Horizontal and vertical wind velocities were calculated on a three-dimensional grid using Doppler winds measured by the NCAR CP-3 and CP-2 radars and the WPL NOAA-C and NOAA-D radars. Wind and reflectivity fields were calculated at four times (1401, 1406, 1414, and 1424 MST) with individual radar scans spanning a period of ±2.5 min of the nominal center time. Scans made at similar elevations were generally made within 90 s of one another. For the first two volume scans, only CP-2 and CP-3 data were available. Low-level (0.5 km AGL) data in the northeast corner of the analysis domain were affected by ground clutter in the CP-2 data. For the last two scans NOAA-C and NOAA-D data were also available, and no significant loss of data due to ground clutter occurred. For the last two volume scans, horizontal winds were calculated in a least-squares sense at each grid point by linearly weighting each radar's contribution by its relative distance. For all scans, vertical velocities were found by iteratively integrating upward the convergence of the horizontal wind, incorporating variations in surface topography.

The analysis grid had a horizontal and vertical spacing of 500 m and consisted of four levels starting at 500 m above the elevation of the CP-3 radar. The grid spacing was chosen to be similar to the coarsest resolution of the four radars (CP-2, ~450 m).

Radar data were first edited to remove ground clutter and spurious velocity data. Next, the data were transformed from radar to Cartesian coordinates using an exponential weighting function with a radius of influence of 500 m. Because no uniform storm motion could be ascribed to the entire analysis, advection corrections were not applied, and the analyses are ground relative. A horizontal data-fill scheme was used before applying a low-pass one-step Leise filter (Leise 1981).

Next, the three-dimensional wind fields were used to calculate terms of the vertical-vorticity equation,

$$\partial\zeta/\partial t = -\mathbf{v}_H\cdot\nabla_H\zeta - w[\partial\zeta/\partial z] - (\zeta + f)(\nabla_H\cdot\mathbf{v}_H) + \boldsymbol{\omega}_H\cdot\nabla_H w \quad (1)$$

where $\zeta = \partial v/\partial x - \partial u/\partial y$ and $\boldsymbol{\omega}_H = (\partial w/\partial y - \partial v/\partial z)\mathbf{i} + (\partial u/\partial z - \partial w/\partial x)\mathbf{j}$ are the vertical and horizontal

components of relative vorticity. Centered differences were used to calculate all derivatives.

a. 1401 MST vorticity analysis

Horizontal winds at 1.0 km AGL and reflectivities near the top of the convective boundary layer (2.0 km AGL) are shown in Fig. 14. A pattern of strong convergence existed, with boundary C separating northerly and southerly flow. The magnitude of the convergence decreased rapidly with height; winds at 1.5 and 2.0 km were more easterly over the analysis domain. Reflectivities reached their maximum values (~15 dBZ) along boundary C. The multiple-Doppler analysis shows that in addition to the boundaries shown in Fig. 12, a weak diverging outflow (dashed line) existed near $(x, y) = (13.0, 12.0)$ km. This outflow appears to have been associated with a convective cell located ~4 km farther east, where near-surface reflectivities reached 30 dBZ at $(x, y) = (17.0, 13.0)$ km at 1354 MST. Surface mesonet potential temperatures and mixing ratios showed only small changes ($\Delta\theta \approx -1.0°C$, $\Delta q \sim +0.5$ g kg^{-1}) as this outflow passed a nearby mesonet station at $(x, y) = (17.1, 11.8)$ km at 1357 MST.

The vertical velocity field at 1.0 km AGL shows rising motion along boundary C and along the leading edge of the outflow. A downdraft was centered in the outflow region, reaching speeds of nearly -4 m s^{-1}. The strongest rising motions existed ahead of the outflow, both along its northern edge and along its southern edge, where it was nearly coincident with the southeastern portion of boundary C.

Contours of vertical vorticity at 1.0 km AGL show that numerous local maxima existed on or near boundary C, with a horizontal spacing of ~3.0 km. Several of these maxima were associated with the azimuthal shear maxima of Fig. 12. An additional local maximum of vorticity existed along the northern side of the outflow boundary at $(x, y) = (11.4, 13.0)$ km.

Inspection of the stretching term shows that at 1401 MST some of the largest local values were associated with the vorticity maxima situated along the southeastern section of boundary C. This increased stretching occurred in the vicinity of the outflow boundary's collision with boundary C, which resulted in increased convergence. Significant stretching also was associated with the vorticity maximum on the north side of the outflow boundary. [The stretching maximum at $(x, y) = (13.2, 12.5)$ km was due to divergence in a region of strong negative vorticity.]

In comparison, the tilting term also shows a region of positive vorticity generation along the outflow boundary. The tilting along the boundary occurred directly upstream of the vorticity maxima at $(x, y) = (11.0, 9.6)$ and $(11.4, 13.0)$ km and had a magnitude similar to the stretching term. Amplitudes of the horizontal-vorticity vector at 1.0 km AGL were ~10 $\times 10^{-3}$ s^{-1}, somewhat larger than the vertical vorticity. To the north of boundary C the horizontal vorticity was generally oriented in a west-southwest streamwise direction, associated with a veering of the wind with height. (Similar vertical shears, due to the overrunning of southeasterly flow above the northeasterly near-surface flow, were found in the case study of a DC by Wilczak and Christian 1990.) Positive tilting occurred as horizontal vorticity, with a component directed across the outflow boundary, was tilted upward by the large vertical velocity gradient across the boundary.

b. 1406 MST vorticity analysis

Evaluation of the horizontal wind and vertical-vorticity fields at 1401 and 1406 MST and single-Doppler radial winds at earlier times suggests that the three local maxima of vorticity at $(x, y) = (8.8, 10.2)$, $(11.0, 9.6)$, and $(11.4, 13.0)$ km at 1401 MST had coalesced near $(x, y) = (9.0, 11.0)$ km 5 min later (Fig. 15). This formed the incipient parent circulation (i.e., the misocyclone) within which the tornado later formed.[3] The diameter of the misocyclone was smaller than 1 km at 0.5 km AGL, increasing to a diameter of ~1 km at 1.0 and 1.5 km AGL. At 2.0 km, the misocyclone did not exist, confirming that the misocyclone began as a low-level circulation. Peak values of vertical vorticity in the misocyclone at 1.0 km reached 14×10^{-3} s^{-1}, nearly three times greater than the 1401 MST peak values. The wind field at 1406 MST also shows that a second vortex had formed at the western edge of the analysis domain on boundary C near $(x, y) = (4.0, 14.0)$ km.

Reflectivity values at 2.0 km AGL had increased rapidly ~8 km north of the misocyclone, reaching 45 dBZ, indicative of rain. At 1.0 km, peak reflectivities remained near 15 dBZ (not shown), indicating that the rain had not yet reached the surface. The line of weak reflectivity at 2.0 km AGL along boundary C had become linked to the new area of reflectivity to the north, forming a hooklike echo pattern. A pronounced indentation in the hook was associated with strong southerly flow just east of the misocyclone. A similar notch was observed in the Grand Island tornado discussed by Fujita (1981).

The 1406 MST vertical velocity field shows the principal updraft, with a peak velocity of 6.3 m s^{-1}, situated on the northwest side of the misocyclone. The region of strongest updraft continued as an arc to the northeast and then to the east of the misocyclone. To the southeast or rear of the misocyclone a downdraft had formed,

[3] The parent circulation is defined as the area with $\zeta \geq 10 \times 10^{-3}$ s^{-1}, the same value as used by Brandes (1984b) in his study of a mesocyclone in a supercell tornadic storm. However, because of the smaller diameter of the 2 July parent circulation, we refer to it as a misocyclone, consistent with the definition of a misocyclone given by Fujita (1981).

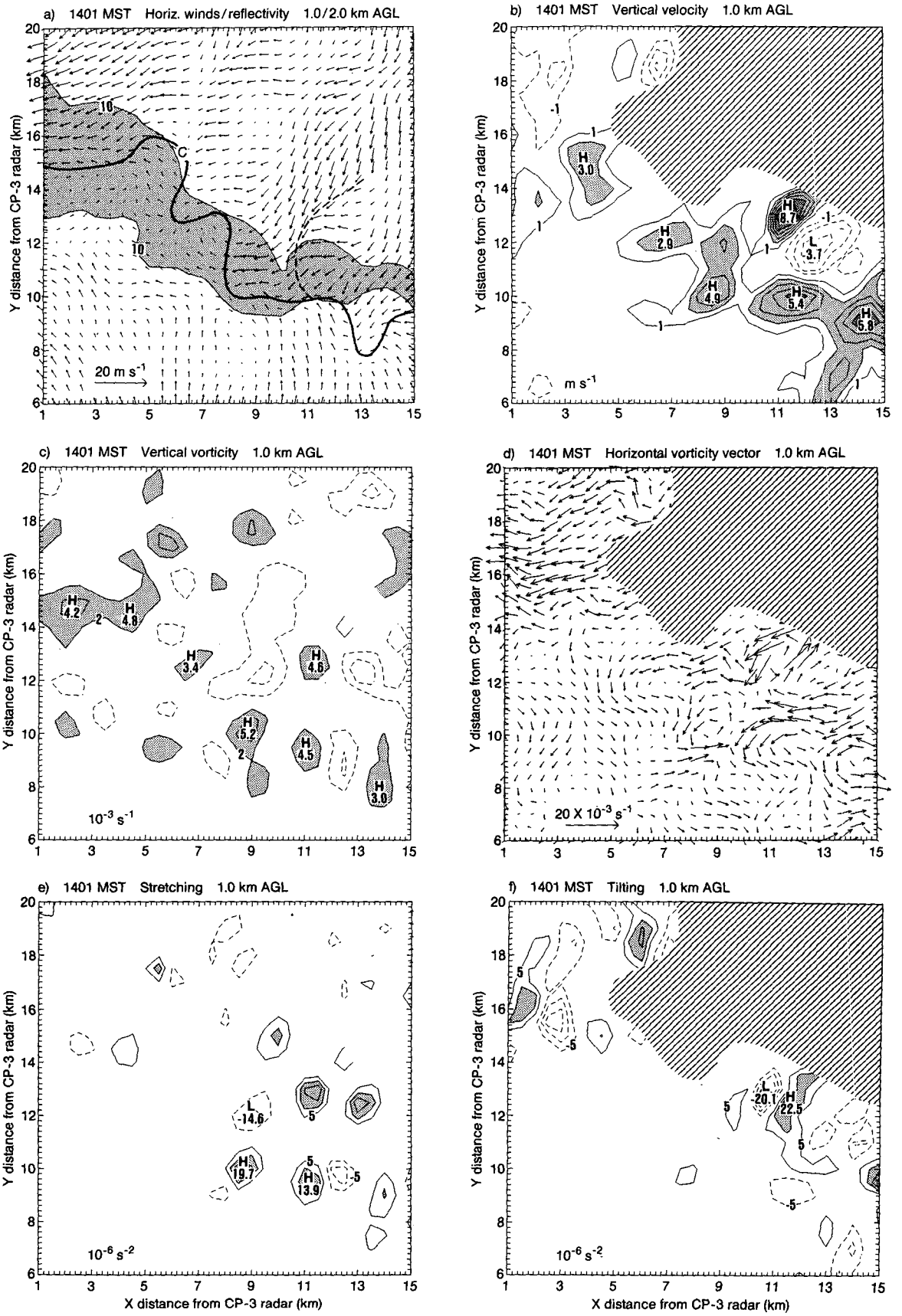

with an amplitude about one-third that of the updraft. The amplitude of the rear downdraft increased with height, reaching -4 m s^{-1} at 2.0 km AGL. The misocyclone was located in the region of large gradient of vertical velocity between the updraft and rear downdraft, slightly toward the updraft side.

In addition to the outflow downdraft to the east and the rear downdraft, a third downdraft is visible approximately 4 km north of the misocyclone at $(x, y) = (9.0, 14.5)$ km. This downdraft was associated with anticyclonic curvature of the wind field and negative vertical vorticity. The downdraft occurred in a region between surface mesonet stations, making it impossible to readily detect any cold outflow boundaries in the surface data.

Inspection of the stretching term at 1.0 km AGL indicates that the maximum value of stretching had increased from 20×10^{-6} s^{-2} at 1401 MST to 31×10^{-6} s^{-2} at 1406 MST. The magnitude of positive stretching at 1406 MST was greatest at 0.5 km AGL (60×10^{-6} s^{-2}) and then decreased rapidly with height, with the net stretching within the misocyclone becoming near zero at 1.5 and 2.0 km. At 0.5 km the peak stretching was collocated with the misocyclone center; however, at 1.0 km and higher levels the position of positive stretching gradually shifted to the north side of the misocyclone, and negative stretching developed on the east-southeast side of the misocyclone due to diverging flow associated with the rear downdraft.

At 1.0 km AGL the tilting term shows a positive peak value very nearly collocated with the misocyclone, with an amplitude two-thirds that of the stretching term. This positive tilting value was associated with northward-oriented ω_H being tilted upward in the region of strong w gradient between the rear downdraft and main updraft. At 1.5 km AGL the net tilting term contribution within the misocyclone was slightly less than at 1.0 km; however, the tilting term at 1.5 km was larger than the stretching term. A second region of positive tilting was still occurring along the outflow boundary to the east. In addition, positive tilting had also developed to the north of the misocyclone; here strong southwestward-oriented streamwise horizontal vorticity, associated with a rapid veering of the horizontal winds, had developed north of the misocyclone. This streamwise vorticity was oriented nearly parallel to the surface buoyancy contours (Fig. 15d).

Finally, vertical advection was found to be a significant loss term at and below 1.0 km AGL in the region of the misocyclone (Fig. 15g). The vertical profile of peak vertical vorticity (Fig. 16) shows at 1406 MST a higher value at 1.5 than at 0.5 km, resulting in negative vertical advection in the misocyclone updraft at 1.0 km. Above 1.0 km the peak vertical vorticity decreased rapidly. Although vertical-vorticity advection was negative at and below 1.0 km, at higher levels it was significantly positive.

c. *1414 MST vorticity analysis*

Between 1406 and 1414 MST the misocyclone propagated $\sim$1.1 km to the north-northwest along boundary C, forming a complete circular vortex (Fig. 17). During this time both the size of the misocyclone and its peak intensity remained nearly constant. The reflectivity field remained relatively unchanged from 1406 MST.

The w and ζ fields at 1414 MST continued to display an arc-shaped pattern to the north and east of the misocyclone. The rear downdraft had weakened, while the negative vertical vorticity associated with the rear downdraft strengthened. The third downdraft, located due north of the misocyclone, propagated southward between 1406 and 1414 MST. Over the preceding 8 min the strength of the misocyclone increased principally at the upper analysis levels (Fig. 16).

By 1414 MST the stretching term at 1.0 km AGL had increased significantly in the region of the misocyclone and dominated the contribution from the tilting term. Stretching in the misocyclone decreased with height, with a maximum value of 71×10^{-6} s^{-2} at 0.5 km. At 0.5 and 1.0 km the stretching term was centered on the misocyclone; above, the stretching maximum was again offset to the north of the misocyclone, with negative stretching to the south. The net stretching within the misocyclone was near zero at 1.5 km and significantly negative at 2.0 km.

Tilting within the misocyclone at 1414 MST had decreased slightly as the gradient of vertical velocity between the rear downdraft and the updraft decreased. Also, the region of positive tilting to the north had weakened. While the stretching term was centered on the misocyclone at 1.0 km AGL, the tilting term was largest on the peripheries of the misocyclone. Like stretching, tilting decreased with height, becoming mostly negative within the misocyclone at 1.5 km. Vertical advection (not shown) continued to be a significant loss term at 1.0 km, but was positive at 1.5 km AGL.

FIG. 14. Low-level Doppler radar analysis at 1401 MST of (a) horizontal winds at 1.0 km AGL, with contours of reflectivity from CP-3 (10-dBZ interval) at 2.0 km AGL, and values greater than 10 dBZ shaded; the surface convergence boundary C (heavy solid line), and the outflow boundary (dashed line); (b) vertical velocity at 1.0 km AGL with a contour interval of 1.0 m s^{-1}; dashed contours are negative and the zero contour is omitted; values greater than 2 m s^{-1} are shaded; (c) vertical vorticity at 1.0 km AGL with a contour interval of 2.0×10^{-3} s^{-1}; values greater than 2×10^{-3} s^{-1} are shaded; (d) the horizontal vorticity vector field at 1.0 km AGL; (e) the stretching term at 1.0 km AGL with a contour interval of 5×10^{-6} s^{-2}; values greater than 10×10^{-6} s^{-2} are shaded; and (f) the tilting term at 1.0 km AGL with a contour interval of 5×10^{-6} s^{-2}. Hatched areas are regions influenced by ground clutter in the 0.5-km AGL wind field.

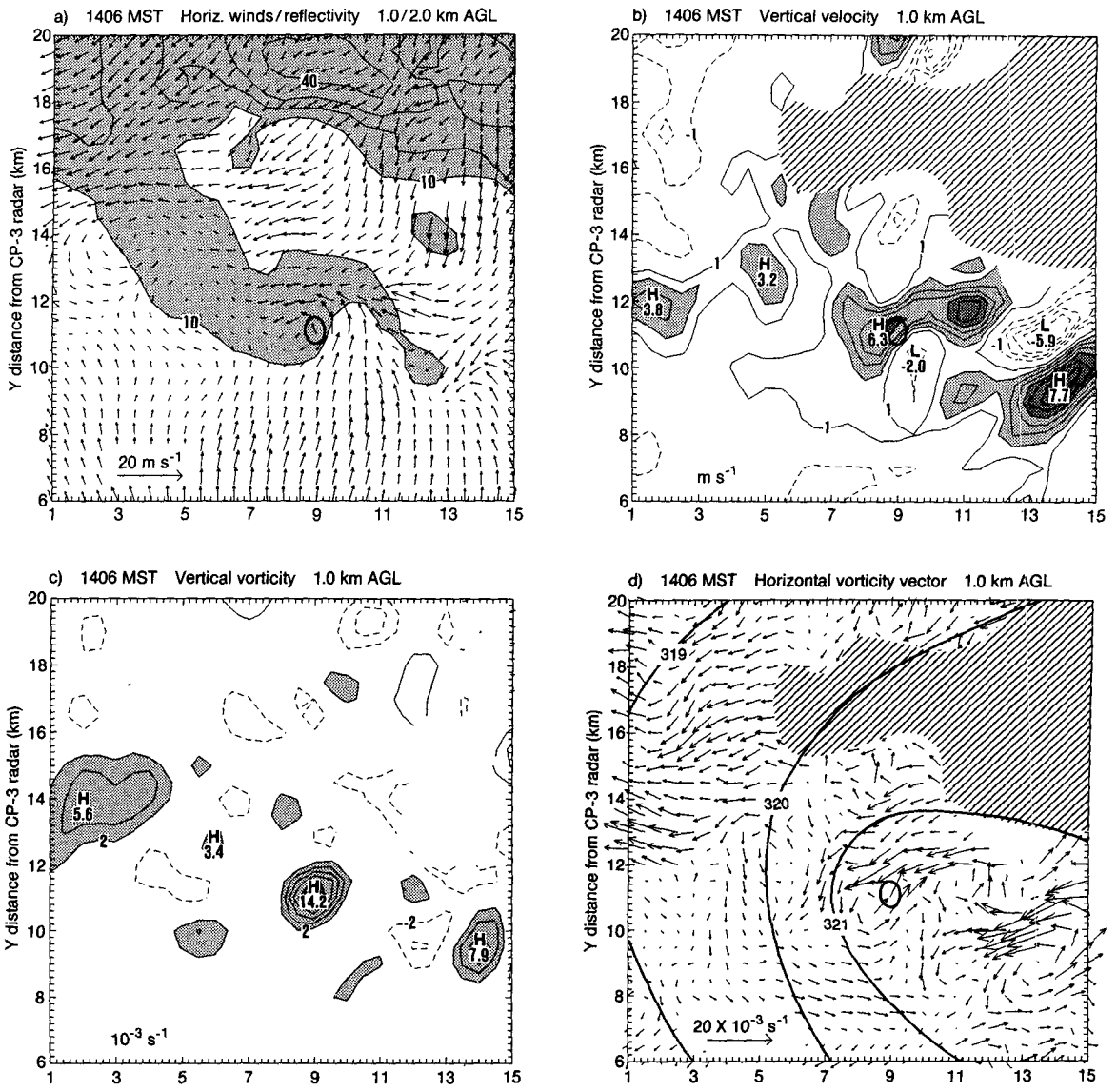

FIG. 15.(a)–(f) As in Fig. 14, but at 1406 MST, with contours of 20-min average surface virtual potential temperature (K) in (d); and (g) the vertical advection term at 1.0 km AGL with a contour interval of 5×10^{-6} s^{-2}. The heavy solid line denotes the misocyclone.

d. 1424 MST vorticity analysis

By 1424 MST, at which time the tornado was just becoming visually apparent, the misocyclone had strengthened and had propagated farther west under the hook echo, which had also amplified considerably (Fig. 18). As in the previous two analysis times, there was an indentation in the hook echo to the east of the misocyclone. The weaker vortex to the west at (x, y) = (3.0, 11.5) km had continued to drift southward.

In comparison with the previous analysis time, at 1424 MST the misocyclone updraft and rear downdraft had weakened. A band of minimum w now wrapped cyclonically from the earlier region of the rear downdraft, around to the east of and into the center of the misocyclone, showing some similarity to the high-resolution model simulations of the mesocyclone occlusion process (Klemp and Rotunno 1983.) The minimum vertical velocity at the vortex center was actually a downdraft of approximately -1 m s^{-1} at 1.5 and 2.0 km AGL. (Finer-scale data analyzed in Part II show subsiding motion taking place within the core of the tornado vortex itself at this time, which later reverses to updraft again.) A broad area of updraft remained in the region surrounding the misocyclone. A temporary weakening of a mesocyclone updraft (although at mid-levels) was also observed in the supercell tornado study of Johnson et al. (1987). The numerical simulation of Rotunno and Klemp (1985) also shows weakening updrafts, which they attribute to a downward pressure

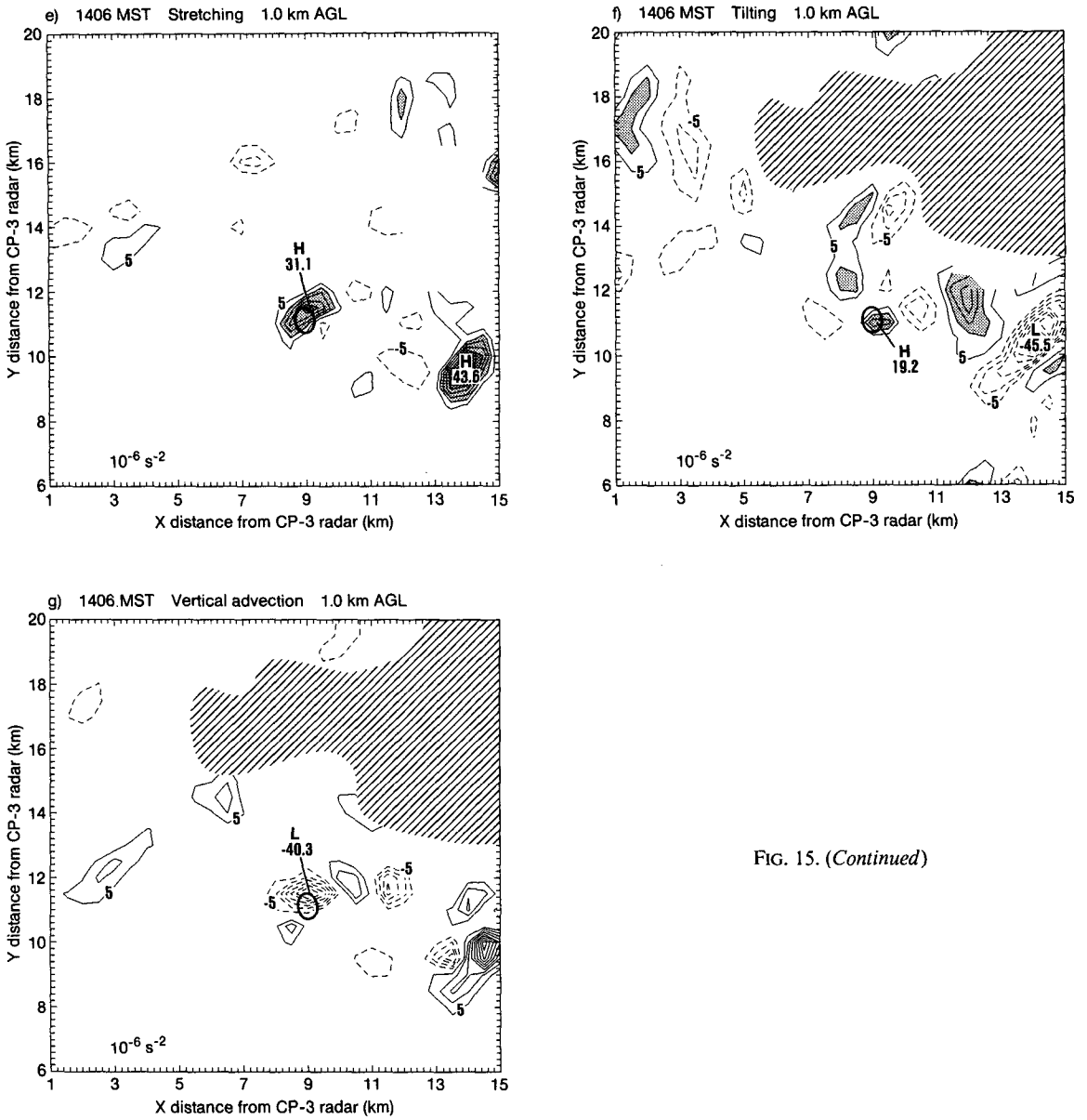

FIG. 15. (*Continued*)

gradient resulting from strong rotation developing near the ground.

At 1424 MST the peak vertical vorticity associated with the misocyclone at 1.0 km AGL had increased by ~40% from the previous analysis time, and the area of the misocyclone also increased. The height of maximum vertical vorticity had risen from 1.0 km at 1406 MST to at least 2.0 km at 1424 MST (Fig. 16). Also, additional local maxima at 1.0 km were associated with the vortex to the west and with the remnants of the arc of enhanced vorticity extending to the east of the misocyclone. The vortex immediately to the west had also increased in intensity even though it was no longer under the hook echo.

As the downdraft in the center of the misocyclone developed, the stretching term decreased, becoming mostly negative at 1424 MST. A region of weaker positive stretching still existed on the peripheries of the misocyclone. At 0.5 km AGL (not shown) the stretching term remained positive within the misocyclone.

By 1424 MST the tilting term at 1.0 km had become generally negative in the region of the misocyclone, in part a consequence of the development of the minimum vertical velocity at the vortex center. Moreover, the horizontal vorticity had decreased in strength in and around the misocyclone as the low-level winds became more uniform with height. At 1.5 km the average contribution of tilting within the misocyclone was near

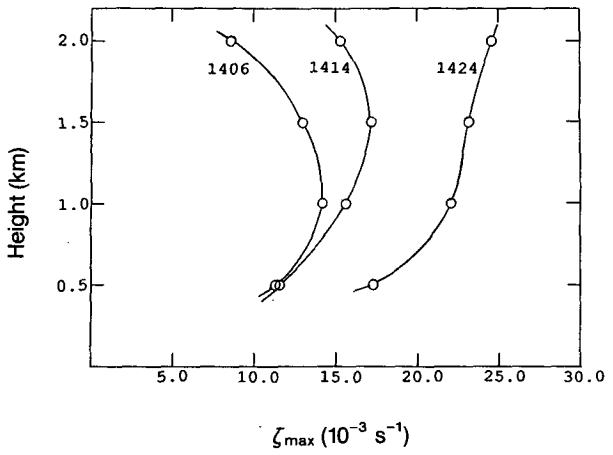

FIG. 16. Vertical profile of maximum vertical vorticity at 1406, 1414, and 1424 MST.

zero. Vertical advection at 1.0 km was again negative, while at 1.5 km it was near zero.

e. Trajectory analysis

Using winds at 1424, 1414, and 1406 MST, backward trajectories have been computed for a series of points that end in the immediate misocyclone vicinity at 1.1 km AGL at 1424 MST (Fig. 19). The trajectories indicate that misocyclone parcels originated at low levels to the north. As these parcels approached the misocyclone they passed through the region of strong baroclinity associated with the DC. On the scale resolved by the relatively coarse grid ($\sim$10 km spacing) of the surface mesonet, gradients of θ_v in the inflow region [$\approx$2.5°C (10 km^{-1})] at 1406 MST were about 50% of those observed in the numerical simulation of a supercell mesocyclone (see Fig. 8d of Rotunno and Klemp 1985); furthermore, the location and orientation of the θ_v contours relative to the trajectories of parcels that converged into the misocyclone are similar to those of the numerical simulation. Parcels traversing this region over a 15-min period would increase their horizontal vorticity by $\sim 8 \times 10^{-3}$ s^{-1}, a value comparable to that observed. These facts suggest that the mechanism for vertical-vorticity generation proposed by Rotunno and Klemp, that is, baroclinic generation of streamwise horizontal vorticity with subsequent tilting and stretching by the storm updraft, was important for the nonsupercell 2 July tornado.

Unfortunately, the resolution of the radar data does not allow for calculation of the tilting term at heights below 1.0 km AGL, where most of the parcels originate. However, at 1.0 km regions of positive tilting were present to the north of the developing misocyclone at 1406 MST, and to a lesser extent at 1414 MST.

We note that many of the parcels flowing into the misocyclone from the north initially had negative vertical vorticity (less than -3×10^{-3} s^{-1}) associated with an anticyclonic turning of the wind present near (x, y) = (9.0, 15.0) (Fig. 15a). Forward trajectories beginning at 1406 MST for low-level parcels (0.5 km AGL) in this negative vorticity region converged into the core of the misocyclone, attaining vertical vorticities greater than 15×10^{-3} s^{-1}. Clearly the positive vertical vorticities of parcels such as these cannot be attained through stretching alone. The trajectories of these parcels show that they traversed the region of positive tilting to the north of the misocyclone in Fig. 15f (although at heights below 1.0 km) and then rose up through the regions of positive tilting immediately surrounding the misocyclone at 1414 MST (Fig. 17f).

7. Summary and discussion

On 2 July, synoptic-scale forcing was weak but tending toward upward vertical motion as the axis of a broad ridge present from the surface through 500 mb passed through eastern Colorado. The approach of a shallow, 700–600-mb short-wave trough resulted in 1°–2°C of cooling aloft that eroded a strong PBL capping inversion that, in part, existed because of an advected mountain boundary layer. The short-wave trough also produced upward motion and positive vorticity advection. An 850-mb thermal–synoptic low amplified over the mountains to the west, resulting in strong southeasterly surface flow. This provided conditions suitable for the formation of a Denver Cyclone, which increased low-level convergence and resulted in increased mesoscale upward vertical motion.

Although the synoptic conditions do not give strong *conventional* indications of severe weather, they do match many of the conditions discussed by Doswell (1980) in his study of synoptic-scale environments associated with High Plains severe thunderstorms. Conditions discussed by Doswell that were present on 2 July include: (a) a 500-mb ridge and moderate ($\geq$10 m s^{-1}) westerly winds over Colorado, (b) marginal instability with lifted indices in the range of $-3°$ to $-1°$C, (c) significant vector shear, (d) an increase in the easterly, afternoon upslope component of the wind from the surface to 850 mb, and (e) surface dewpoint temperatures $\geq$ 7°C.

Low-level convergence boundaries, associated with the Denver Cyclone, were present on 2 July 1987. Weak, small-scale vortices frequently occur along Denver Cyclone convergence boundaries; however, it is only when synoptic conditions conducive to High Plains severe weather are also present that these vortices are likely to develop into tornadoes.

A dominant feature of the near-surface flow on 2 July was the presence of boundary C, a stationary convergence line that appears to have developed due to the local topography and evolving DC flow. Numerous small vortices, visible as regions of enhanced azimuthal shear in the low-level CP-3 Doppler data, formed along

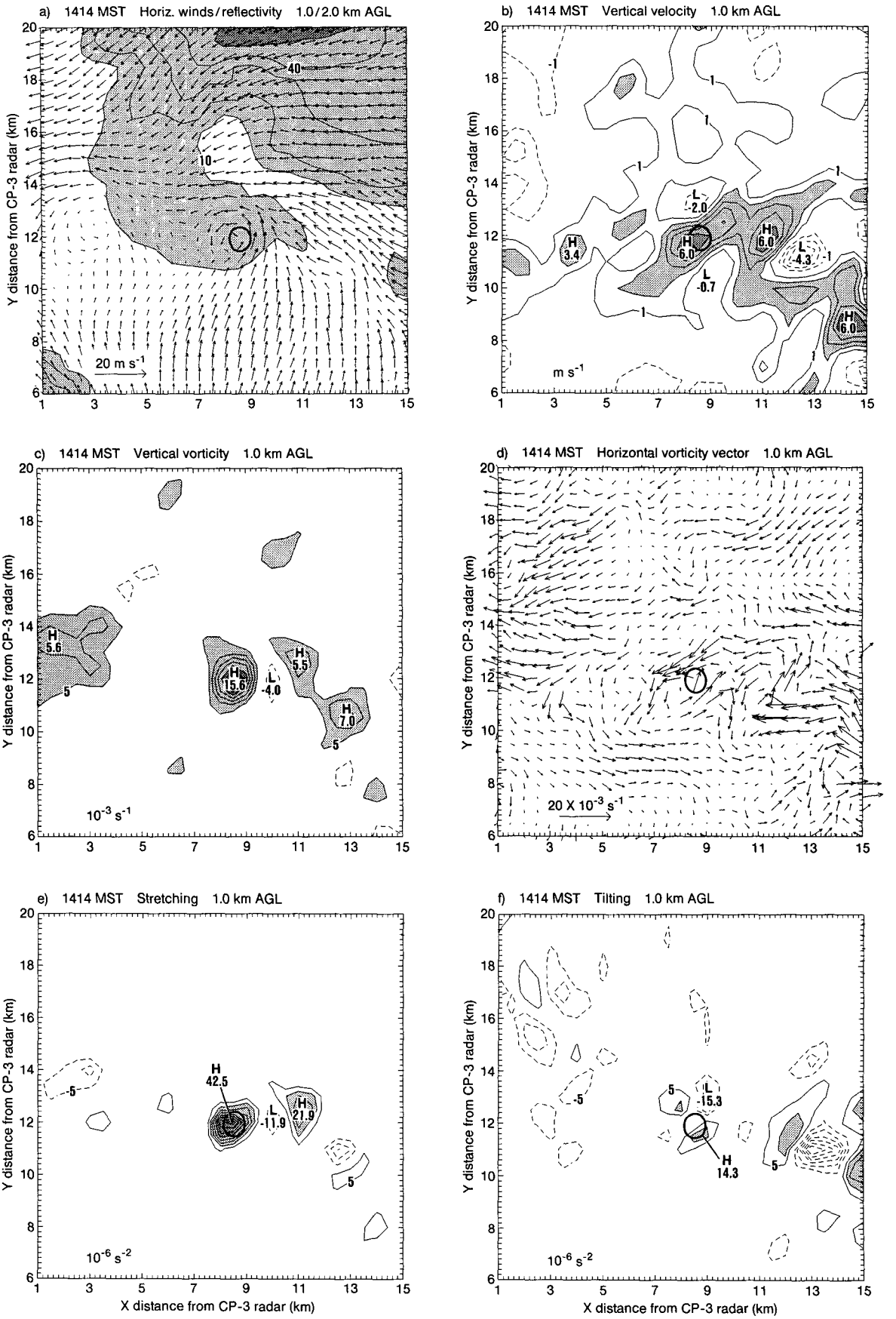

FIG. 17. As in Fig. 14, but at 1414 MST.

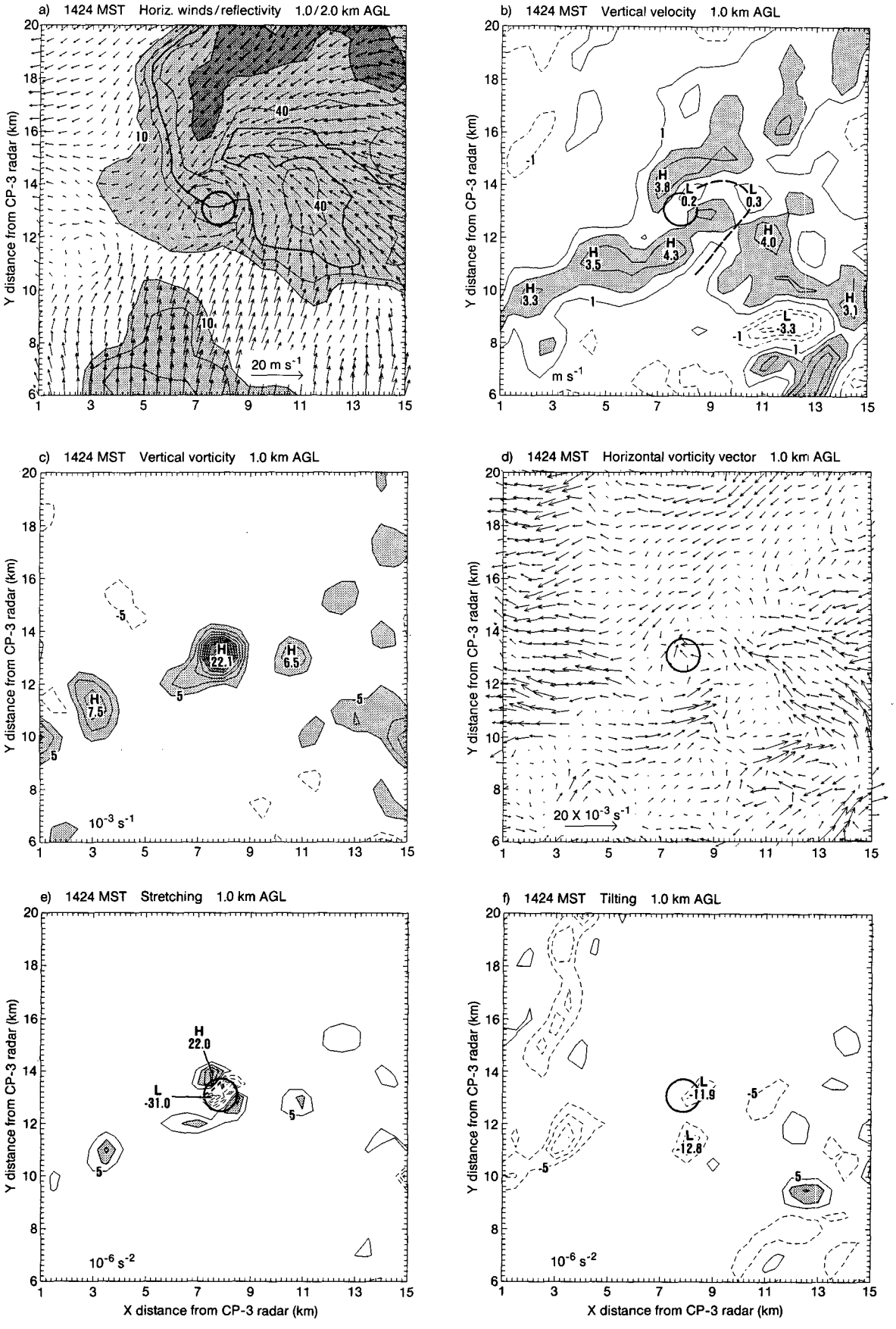

FIG. 18. As in Fig. 14, but at 1424 MST. The dashed line in (b) indicates a band of minimum vertical velocity.

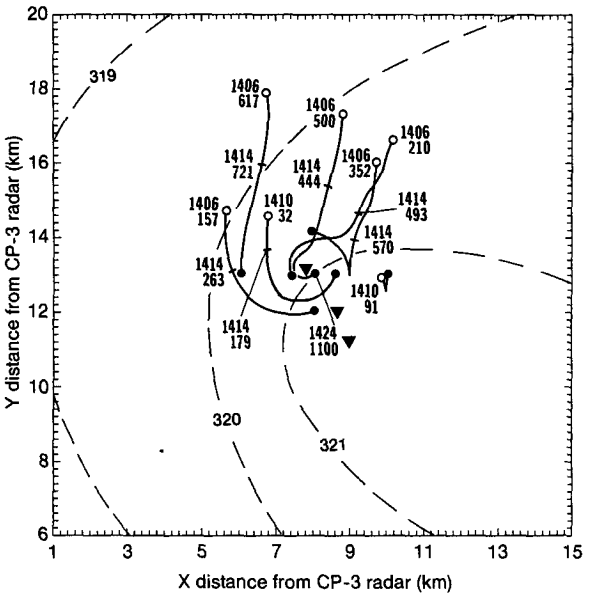

FIG. 19. Trajectories of parcels (solid lines) between 1406 and 1424 MST. Solid circles show final positions at 1.0 km AGL at 1424 MST; open circles show beginning locations. Parcel heights (m AGL) are shown at selected times. Dashed lines show contours of surface virtual potential temperature at 1406 MST as in Fig. 15. Misocyclone positions at 1406, 1414, and 1424 MST are indicated by triangles.

boundary C and slowly propagated northwestward. The horizontal spacing of these vortices (~3 km) was similar to the depth of the convective boundary layer. Because of the small dimensions of these vortices in their developing stages, the radar data could not resolve the mechanisms that contributed to their generation.

A band of enhanced radar reflectivities reaching ~15 dBZ was associated with boundary C. Later, a convective cell from a region of multicellular convection to the north developed southward, linking up with the reflectivity band on boundary C to form a hooklike-echo appendage. The evolution of the hook echo was atypical, in that the hook appendage long preceded the generation of the main cell to which it was later attached.

At 1401 MST, a weak outflow boundary (originating from a cell different from the one that would append the hook echo) was colliding with boundary C. Along the outflow boundary, horizontal vorticity was tilted into positive vertical vorticity and stretching increased, which intensified several small vortices. Two of the vortices on boundary C then merged with a third vorticity maxima on the northern edge of the outflow boundary, producing the incipient misocyclone within which the 2 July tornado later formed.

At 1406 MST, as the low-level rotation increased in intensity to form the misocyclone, a rear downdraft developed simultaneously to the southeast of the misocyclone. In contrast to the supercell tornadic storm structure proposed by Lemon and Doswell (1979), a large-scale rear-flank downdraft was not observed. Instead, the rear downdraft was similar in its location relative to the misocyclone and in its size to the rear downdrafts observed by Brandes (1984b) in the Del City and Harrah supercell tornadoes, and to the occlusion downdraft observed in the model results of Klemp and Rotunno (1983).

The rear downdraft at 1406 MST created a large horizontal gradient of vertical velocity that allowed for the tilting of horizontal vorticity in the southeastern portion of the misocyclone. At 1.5 km AGL, tilting was larger than the stretching associated with the misocyclone. Though the rear downdraft was important in the tilting of horizontal vorticity, it also strengthened the low-level stretching in the vicinity of the misocyclone through increased convergence along the leading edge of the downdraft.

At both 1406 and 1414 MST a third downdraft was present to the north of the misocyclone. This forward downdraft was not in a region of high reflectivity, but instead was situated under the weaker-reflectivity region near the hook echo. Therefore, it appears to be fundamentally different from the rainy downdrafts observed ahead of supercell mesocyclones (Brandes 1984b).

Additional positive tilting occurred at 1406 MST to the northwest of the misocyclone, in a region of strong baroclinity. A trajectory analysis shows that inflow into the base of the misocyclone came from the north, with parcels developing streamwise horizontal vorticity as they passed through the baroclinic region. The positive tilting to the north of the misocyclone occurred as parcels with significant streamwise vorticity entered the updraft surrounding the misocyclone, in a manner very similar to that proposed by Rotunno and Klemp (1985) for supercell tornadoes. An important difference, however, is that on 2 July the baroclinic generation resulted from preexisting buoyancy gradients associated with the Denver Cyclone, and not from gradients generated by the storm itself.

Between 1406 and 1414 MST the misocyclone propagated northwestward along the convergence boundary. At these two analysis times the average stretching term within the misocyclone was most strongly positive at the lower levels (0.5 and 1.0 km), becoming small or even negative at 1.5 and 2.0 km. Tilting also decreased at 1.5 km relative to 1.0 km. Thus, most of the vertical-vorticity generation occurred at heights at and below 1.0 km AGL. At greater heights the increase of vertical vorticity appears to have been mainly due to vertical advection.

By 1424 MST, the tornado had just become visible as a rotating dust cloud on the ground. The strength of the misocyclone had increased significantly; however, updrafts in the vicinity of the misocyclone had weakened substantially. [Similar observations of supercell tornadoes occurring only after updrafts began to weaken led Lemon and Doswell (1979) to conclude that stretching alone was unlikely to result in torna-

dogenesis.] In addition, at 1424 the rear downdraft had weakened and formed a band of minimum w that wrapped cyclonically around and into the region of the misocyclone, showing some similarities to numerical simulations of a supercell in its occlusion stage (Klemp and Rotunno 1983). Observations of supercell storms suggest that tornadogenesis occurs during the occlusion stage (Lemon and Doswell 1979; Burgess et al. 1976; Burgess et al. 1977; Brandes 1977, 1978).

Although the 2 July tornado did not have a precursor supercell nor mesocyclone, its similarities to mesocyclone tornadoes are striking. For comparison, we cite the detailed vorticity analysis of the Del City supercell tornado by Brandes (1984b). This same storm was modeled by Klemp and Rotunno (1983). Taking into account the northward propagation of the Del City mesocyclone versus the northwestward propagation of the 2 July misocyclone, we compare the structure of the tornadic phase of the Del City storm (Brandes 1984b, Fig. 5) with the present analysis. The similarities include:

1) arc-shaped updraft and vertical-vorticity fields, extending out on the right flank of the misocyclone (1406–1414 MST);
2) the misocyclone located on the updraft side of the region of strongest vertical velocity gradient (1406 MST);
3) a rear downdraft forming in the notch of the arc (1406–1414 MST);
4) negative ζ associated with the rear downdraft (1414 MST);
5) the strongest ω_H on the forward right flank of the misocyclone, oriented across the direction of misocyclone propagation (1406 MST);
6) the maximum tilting collocated with the misocyclone center, with additional tilting ahead and on the right flank of the misocyclone (1406 MST);
7) the stretching term initially positive near the vortex center (1406–1414 MST), later developing a positive–negative structure within the misocyclone as the main updraft weakens (1424 MST).

A difference that exists between this case and that of Brandes (1984b) concerns timing. At the time of Brandes' Fig. 5, a tornado was present. For the plots that exist between 1406 and 1414 MST in this study, a visible tornado had yet to form.

The vorticity budget analysis indicates that significant tilting of horizontal vorticity did occur in this case, as was also found by Carbone (1983) in a vorticity budget analysis for a cold-frontal, nonsupercell tornado. The role of tilting is the primary distinction between supercell tornado theory and nonsupercell tornado theory. Although for supercell–mesocyclone tornadoes it is stretching that ultimately intensifies the tilted vorticity into the tornado, tilting must occur in order for vertical vorticity to be present and stretched. In nonsupercell tornado theory, tilting is not a necessary ingredient for tornadogenesis.

Vorticity associated with the 2 July 1987 nonsupercell tornado was generated in a more complicated manner than that proposed by Brady and Szoke (1989) and by WW89. Although stretching of preexisting vorticity clearly was occurring, trajectory and vorticity analyses indicate that the strengthening of the misocyclone through the tornado formation stage was dependent on the tilting process. Tilting was present in the vicinity of the misocyclone for 25 min prior to tornado formation, with a magnitude at times nearly equal to that of stretching. Furthermore, the generation of horizontal vorticity and its subsequent tilting shared many of the characteristics of supercell tornadogenesis.

The supercell–mesocyclone tornadogenesis theory of Klemp and Rotunno (1983) suggests that the generation of vorticity aloft may be distinct from the generation of vorticity near the surface. Johnson et al. (1987) conclude from observations of supercell–mesocyclone tornadoes that the mechanism that initiates low-level rotation is in fact different from that at midlevels. Also, Rotunno (1986) argues that the appearance of a preceding tornado vortex signature aloft may not be relevant to the development of a visible funnel in contact with the ground. The 2 July observations indicate that the near-surface mechanism of Rotunno and Klemp (1985) played an important role in forming the large vertical vorticities within the tornado parent vortex. This was made possible by the presence of an environment similar to that generated within supercell storms, without, however, a supercell or midlevel rotation being present. Features of this environment included a surface convergence boundary, strong baroclinity, streamwise horizontal vorticity, and positive vertical vorticity. These features, resulting from the development of the Denver Cyclone, appear to have acted as surrogates for similar structures occurring within supercell thunderstorms.

Model simulations by Walko (1990) of vortex development along shear lines suggest that it is, nevertheless, possible for tornadolike vortices to be generated solely by the stretching mechanism. However, in his simulations the initial vertical vorticity associated with the shear line [$\sim$20 m s^{-1} (3 km)$^{-1}$] was nearly an order of magnitude larger than the mean horizontal shear along boundary C observed shortly before misocyclone formation on 2 July.

Brady and Szoke (1989) suggest that their proposed nonsupercell mechanism is similar to that of waterspout formation (e.g., Golden 1974a,b; Simpson et al. 1986). However, because of a lack of adequate measurements, the exact mechanism of waterspout formation remains obscure. Circumstantial evidence suggests that the difference between tornadoes and waterspouts may not be fundamental, but rather one of scale and intensity (Golden and Purcell 1978). Numerical simulations by Simpson et al. (1986) indicate that low-

level vertical shear associated with gust fronts is important for the formation of near-surface vorticity in waterspouts—thereby implying that tilting is important. The development of the 2 July tornado has many of the broad characteristics of waterspout formation, and yet in its detail also has similarities to supercell–mesocyclone tornado formation.

Finally, we note that because most nonsupercell–mesocyclone tornadoes occur along storm outflow gust fronts, cold fronts, or stationary convergence lines, which typically have significant baroclinity associated with them, large vertical shears (horizontal vorticity) will exist in their vicinity. Therefore, it seems plausible that the tilting of baroclinically produced horizontal vorticity may play an important role in other examples of nonsupercell–mesocyclone tornadoes.

Acknowledgments. The authors wish to thank Tom Matejka for providing the trajectory analysis program, John M. Brown for his assistance with the QG analysis, Brooks Martner, Taneil Uttal, and Roger Wakimoto for their helpful discussions, and Robert Davies-Jones and an anonymous reviewer for their constructive comments. The authors are also grateful to Robert Kropfli, L. Jay Miller, Chris Burghart, and Dick Oye for their suggestions regarding processing of the radar data, and to Mark Govett for his assistance in running the trajectory analysis program.

APPENDIX A

PAM Thermodynamic Bias Corrections

During the course of the CINDE field program, intercomparison tests were made between the PAM thermodynamic sensors and a standard, well-calibrated psychrometer. These tests, made on approximately five different days spanning the course of the experiment, revealed consistently high wet-bulb biases in the PAM data, with a mean offset of +0.6°C and a standard deviation of 0.3°C. PAM technical personnel have since attributed these biases to insufficient ventilation of the PAM wet bulb. Low biases in the PAM dry-bulb temperature were also observed, with a mean of −0.31°C and a standard deviation of 0.21°C. The PAM errors showed no clear trend with time. Therefore, to correct for the biases, each PAM station's temperature and wet-bulb temperature were adjusted by the average correction determined for each separate PAM during the experimental period.

APPENDIX B

Mobile Sounding RH Corrections

Intercomparisons made during and after CINDE with the mobile radiosonde and CLASS soundings, Boulder Atmospheric Observatory (BAO) tower data, and aircraft data show a consistent relative humidity (RH) bias in the mobile soundings of approximately −4% RH, for RH < 65%. Consequently, RHs in this range have been adjusted to account for the observed error.

An RH bias in carbon hygristor sensors similar to those used in the mobile soundings has also been observed elsewhere (Williams and Acheson 1976), where it was attributed to the thermal lag of the relatively bulky hygristor relative to the temperature measured by the thermistor that is used to calculate RH. This thermal lag will result in a negative RH bias, with the magnitude depending on the lapse rate and balloon-rise rate. Williams and Acheson evaluated this thermal lag effect for soundings from the Global Atmospheric Research Project (GARP) Atlantic Tropical Experiment (GATE) and concluded that it resulted in an ~5% underestimation of RH, similar to that found in the CINDE data, suggesting that this is a possible source of the observed error. However, the reason for the elimination of the bias for RH > 65%, which was not observed in the GATE data, remains unclear, suggesting the problem may be more complicated. The CLASS soundings use a humicap sensor with a mass that is orders of magnitude less than that of the hygristor and should not suffer from a significant thermal lag problem.

REFERENCES

Barnes, S. L., 1970: Some aspects of a severe, right-moving thunderstorm deduced from mesonetwork rawinsonde observations. *J. Atmos. Sci.*, **27**, 634–648.

——, 1985: Omega diagnostics as a supplement to LFM/MOS guidance in weakly forced convective situations. *Mon. Wea. Rev.*, **113**, 2122–2141.

Benjamin, S. G., and T. N. Carlson, 1986: Some effects of surface heating and topography on the regional severe storm environment. Part I: Three-dimensional simulations. *Mon. Wea. Rev.*, **114**, 307–329.

Blanchard, D. O., and K. W. Howard, 1986: The Denver hailstorm of 13 June 1984. *Bull. Amer. Meteor. Soc.*, **67**, 1123–1131.

Brady, R. H., and E. J. Szoke, 1989: A case study of nonmesocyclone tornado development in Northeast Colorado: Similarities to waterspout formation. *Mon. Wea. Rev.*, **117**, 843–856.

Brandes, E. A., 1977: Gust front evolution and tornadogenesis as viewed by Doppler radar. *J. Appl. Meteor.*, **16**, 333–338.

——, 1978: Mesocyclone evolution and tornadogenesis: Some observations. *Mon. Wea. Rev.*, **106**, 995–1011.

——, 1984a: Relationships between radar-derived thermodynamic variables and tornadogenesis. *Mon. Wea. Rev.*, **112**, 1033–1052.

——, 1984b: Vertical vorticity generation and mesocyclone sustenance in tornadic thunderstorms: The observational evidence. *Mon. Wea. Rev.*, **112**, 2753–2269.

Browning, K. A., and C. R. Landry, 1963: Airflow within a tornadic storm. Preprints, *Tenth Weather Radar Conf.*, Washington, D.C., Amer. Meteor. Soc., 116–122.

Burgess, D. W., L. D. Hennington, R. J. Doviak, and P. S. Ray, 1976: Multimoment Doppler display for severe storm identification. *J. Appl. Meteor.*, **15**, 1302–1306.

——, R. A. Brown, L. R. Lemon, and C. R. Safford, 1977: Evolution of a tornadic thunderstorm. Preprints, *Tenth Conf. on Severe Local Storms*, Omaha, Amer. Meteor. Soc., 84–89.

——, and R. J. Donaldson, 1979: Contrasting tornado storm types. Preprints, *11th Conf. on Severe Local Storms*, Kansas City, Amer. Meteor. Soc., 189–192.

Carbone, R. E., 1983: A severe frontal rainband. Part II: Tornado parent vortex circulation. *J. Atmos. Sci.*, **40,** 2639–2654.

Carlson, T. N., S. G. Benjamin, and G. S. Forbes, 1983: Elevated mixed layers in the regional severe storm environment: Conceptual model and case studies. *Mon. Wea. Rev.*, **111,** 1453–1473.

Davies-Jones, R., 1984: Streamwise vorticity: The origin of updraft rotation in supercell storms. *J. Atmos. Sci.*, **41,** 2991–3006.

——, 1986: Tornado dynamics. *Thunderstorm Morphology and Dynamics.* E. Kessler, Ed., Univ. of Oklahoma Press, 197–236.

——, D. Burgess, and M. Foster, 1990: Test of helicity as a tornado forecast parameter. Preprints, *16th Conference on Severe Local Storms,* Kananaskis Park, Alberta, Canada, Amer. Meteor. Soc., 588–592.

Doswell, C. A., III, 1980: Synoptic-scale environments associated with High Plains severe thunderstorms. *Bull. Amer. Meteor. Soc.*, **61,** 1388–1399.

Dunn, L. B., 1990: Two examples of operational tornado warnings using Doppler radar data. *Bull. Amer. Meteor. Soc.*, **71,** 145–153.

Fankhauser, J. C., and C. Wade, 1982: The environment of the storms. *Hailstorms of the Central High Plains. Vol I: The National Hail Research Experiment.* Colo. Assoc. Univ. Press, 5–32.

Fujita, T. T., 1981: Tornadoes and downbursts in the context of generalized planetary scales. *J. Atmos. Sci.*, **38,** 1511–1534.

Golden, J. H., 1974a: The life cycle of Florida Keys' waterspouts. *J. Appl. Meteor.*, **13,** 676–692.

——, 1974b: Scale interactions for the waterspout life cycle. *J. Appl. Meteor.*, **13,** 693–709.

——, and D. Purcell, 1978: Life cycle of the Union City Oklahoma tornado and comparison with waterspouts. *Mon. Wea. Rev.*, **106,** 3–11.

Holton, J. R., 1979: *An Introduction to Dynamic Meteorology.* Academic Press, 391 pp.

Hoskins, B. J., and M. A. Pedder, 1980: The diagnosis of middle latitude synoptic development. *Quart. J. Roy. Meteor. Soc.*, **106,** 707–719.

Johnson, K. W., P. S. Ray, B. C. Johnson, and R. P. Davies-Jones, 1987: Observations related to the rotational dynamics of the 20 May 1977 tornadic storms. *Mon. Wea. Rev.*, **115,** 2463–2478.

Klemp, J. B., and R. Rotunno, 1983: A study of the tornadic region within a supercell storm. *J. Atmos. Sci.*, **40,** 359–377.

Lazarus, S. M., and K. K. Droegemeier, 1990: The influence of helicity on the stability and morphology of numerically simulated storms. Preprints, *16th Conference on Severe Local Storms,* Kananaskis Park, Alberta, Canada, Amer. Meteor. Soc., 269–274.

Leise, J. A., 1981: A multidimensional scale-telescoped filter and data extension package. NOAA Tech. Memo. ERL WPL-82, NOAA Wave Propagation Laboratory, Boulder, CO, 20 pp. [NTIS PB82-164104.]

Lemon, L. R., and C. A. Doswell III, 1979: Severe thunderstorm evolution and mesocyclone structure as related to tornadogenesis. *Mon. Wea. Rev.*, **107,** 1184–1197.

Lemone, M. A., 1976: Modulation of turbulence energy by longitudinal rolls in an unstably stratified planetary boundary-layer. *J. Atmos. Sci.*, **33,** 1308–1320.

Lilly, D. K., 1982: The development and maintenance of rotation in convective storms. *Intense Atmospheric Vortices,* L. Bengtsson and J. Lighthill, Eds., Springer-Verlag, 149–160.

Maddox, R. A., 1976: An evaluation of tornado proximity wind and stability data. *Mon. Wea. Rev.*, **104,** 133–142.

Rotunno, R., 1986: Tornadoes and tornadogenesis. *Mesoscale Meteorology and Forecasting.* P. S. Ray, Ed., Amer. Meteor. Soc., 414–436.

——, and J. Klemp, 1985: On the rotation and propagation of simulated supercell thunderstorms. *J. Atmos. Sci.*, **42,** 271–292.

Simpson, J., B. R. Morton, M. C. McCumber, and R. S. Penc, 1986: Observations and mechanisms of GATE waterspouts. *J. Atmos. Sci.*, **43,** 754–782.

Szoke, E. J., 1991: Eye of the Denver Cyclone. *Mon. Wea. Rev.*, **119,** 1283–1292.

——, and R. H. Brady, 1989: Forecasting implications of the 26 July 1985 northern Colorado tornadic thunderstorm case. *Mon. Wea. Rev.*, **117,** 1834–1860.

——, and J. A. Augustine, 1990: A decade of tornado occurrence associated with a surface mesoscale flow feature—the Denver Cyclone. Preprints, *16th Conference on Severe Local Storms,* Kananaskis Park, Alberta, Canada, Amer. Meteor. Soc., 554–559.

——, M. L. Weisman, J. M. Brown, F. Caracena, and T. W. Schlatter, 1984: A subsynoptic analysis of the Denver tornadoes of 3 June 81. *Mon. Wea. Rev.*, **112,** 790–808.

Wakimoto, R. M., and B. E. Martner, 1992: Observations of a Colorado Tornado. Part II: Combined photogrammetric and Doppler radar analysis. *Mon. Wea. Rev.*, **120,** 522–543.

——, and J. W. Wilson, 1989: Non-supercell tornadoes. *Mon. Wea. Rev.*, **117,** 1113–1140.

Walko, R. L., 1990: Generation of tornado-like vortices in nonaxisymmetric environments. Preprints, *16th Conference on Severe Local Storms,* Kananaskis Park, Alberta, Canada, Amer. Meteor. Soc., 583–587.

Wilczak, J. M., and T. W. Christian, 1990: Case study of an orographically induced, mesoscale vortex (Denver Cyclone). *Mon. Wea. Rev.*, **118,** 1082–1102.

——, and J. W. Glendening, 1988: Observations and mixed-layer modeling of a terrain induced mesoscale gyre: The Denver Cyclone. *Mon. Wea. Rev.*, **116,** 2688–2711.

Williams, S. L., and D. T. Acheson, 1976: Thermal time constant of the U.S. radiosonde sensors used in GATE. NOAA Tech. Memo. EDS CEDDA-7, 16 pp. [NTIS PB257 367-3G1.]

Wilson, J. W., 1986: Tornadogenesis by non-precipitation induced wind shear lines. *Mon. Wea. Rev.*, **114,** 270–284.

——, and W. Schreiber, 1986: Initiation of convective storms at radar-observed boundary-layer convergence lines. *Mon. Wea. Rev.*, **114,** 2516–2536.

——, J. A. Moore, G. B. Foote, B. Martner, A. R. Rodi, T. Uttal, and J. M. Wilczak, 1988: Convection Initiation and Downburst Experiment (CINDE). *Bull. Amer. Meteor. Soc.*, **69,** 1328–1348.

Zamora, R. J., M. A. Shapiro, and C. A. Doswell III, 1987: The diagnosis of upper tropospheric divergence and ageostrophic wind using profiler wind observations. *Mon. Wea. Rev.*, **115,** 871–884.